

1

Title:

2 **Enhancing environmental models with a new downscaling method**
3 **for global radiation in complex terrain**

4 **Authors / co authors:**

5 Arsène Druel, ~~Arsène~~¹, Julien Ruffault, ~~Julien~~¹, Hendrik Davi, ~~Hendrik~~¹, André Chanzy,
6 André², Olivier Marloie, ~~Olivier~~¹, Miquel De Cáceres, ~~Miquel~~³, Albert Olioso¹, Florent Mouillot,
7 Florent⁴, Christophe François, ~~Christophe~~⁵, Kamel Soudani, ~~Kamel~~⁵, and Nicolas K. Martin-
8 StPaul, ~~Nicolas K.~~¹.

9 ¹ URFM, INRAE, 84000 Avignon, France; ² UMR 1114 EMMAH, INRAE, Avignon University,
10 84000 Avignon, France; ³ CREAM, Centre de Recerca Ecològica i Aplicacions Forestals,
11 Bellaterra, Catalonia, Spain; ⁴ UMR 5175 CEFE, Montpellier University, CNRS, EPHE, IRD,
12 Montpellier, France; ⁵ UMR 8079 ESE, UPS, CNRS, AgroParisTech, Orsay, France

13 **Correspondence email:** arsene.druel@inrae.fr

14 -

15 **Abstract:**

16 Global radiation is a key climate input in forest process-based models (PBM) as it
17 determines photosynthesis, transpiration and the canopy energy balance. While radiation is
18 highly variable at fine spatial resolution in complex terrain due to shadowing effects, data
19 required for PBM currently available over large extents are generally at spatial resolution
20 coarser than ~9 km. Downscaling radiation from large-scale to high resolution available from
21 digital elevation models is therefore of potential importance to refine global radiation
22 estimates and improve PBM estimations. In this study, we ~~introduced~~introduce a new
23 downscaling model that aims to refine sub-daily global radiation data obtained from climate
24 reanalysis or projection at large scales to the resolution of a given digital elevation model.
25 First, downscaling involves splitting radiation into direct and diffuse fraction. Then, the
26 influence of surrounding mountains' shade on direct radiation and the “bowl” (deep valley)
27 effect (~~or skyview factor~~) on diffuse radiation is considered. The model was evaluated by
28 comparing simulated and observed radiation at the Mont Ventoux mountain study site
29 (southeast of France) using the recent ERA5-Land hourly data available at 9 km resolution
30 as input and downscaled at different spatial resolution (from 1 km to 30 m resolution) using a
31 digital elevation model. The downscaling algorithm improved the reliability of radiation at the
32 study site in particular at scales below 150 m. Finally, by using two different process based
33 models (~~CASTANEA~~Castanea, a process-based model simulating tree growth, and SurEau,
34 a plant-hydraulic model simulating hydraulic failure risk), we showed that accounting for fine
35 resolution radiation can have a great impact on predictions of forest ~~functioning.~~ functions
36 ~~and climatic risks.~~

37 **short summary:**

38 Accurate radiation data are essential for ~~the understanding of ecosystem functioning and~~
39 ~~dynamics~~understanding ecosystem growth. Traditional large-scale data lack the precision
40 needed for complex terrains, ~~e.g. mountainous regions~~. This study introduces a new model
41 to enhance radiation data resolution using elevation maps, which accounts for sub-daily
42 direct and diffuse radiation effects caused by terrain features. Tested on ~~a mountainous~~
43 ~~area~~Mont Ventoux, this method significantly ~~improved~~improves radiation estimates,
44 benefiting ~~predictions of forest functioning~~forest growth and climate risk models.

45 1. INTRODUCTION

46 Studies assessing the impacts of climate change on forest ecosystem functions increasingly
47 rely on high resolution spatial and temporal climate data. For example, process-based
48 models that aim to evaluate the effect of climate on forest functions and services require
49 daily or sub-daily temporal resolution meteorology as input (e.g., Davi et al., 2006; De
50 Cáceres et al., 2023; Granier et al., 2007; Ruffault et al., 2013, 2022, 2023) to simulate key
51 ecophysiological processes (transpiration, photosynthesis or water potential). Yet, even
52 relatively fine-grained (*i.e.*, 1 km) historical or projected climate products (Hijmans et al.,
53 2005; Brun et al., 2022) do not correspond to the "topographic scale" and cannot reproduce
54 fine-scale patterns observed in heterogeneous landscapes. Moreover, employing spatially-
55 coarse climatic projections can lead to biased~~biased~~ and irrelevant inferences of local
56 ecological patterns (Bedia et al., 2013) or to substantial errors in impact studies (e.g.,
57 Patsiou et al., 2014; Randin et al., 2009). Improving methodologies to provide climatic data
58 at high spatio-temporal resolution variation is therefore crucial to better understand and
59 predict~~forecast~~ the spatial heterogeneity in forest structure and functions.

60 Among climate variables, radiation is a key driver of plant functioning and productivity
61 globally (Churkina and Running, 1998), acting through ~~though~~ two main mechanisms. On
62 one hand, global radiation determines the photosynthetically active radiation (PAR), *i.e.*, the
63 available energy for photosynthesis and thus plant productivity. Numerous studies have
64 shown the relationship between the amount of solar radiation and the distribution of plant
65 species or communities worldwide (Dirnbock et al., 2003; Franklin, 1998; Meentemeyer et
66 al., 2001; Tappeiner et al., 1998; Zimmermann and Kienast, 1999). On the other hand, the
67 radiation reaching a vegetation surface is an important component of the canopy energy
68 balance, driving surface temperature and vapour pressure deficit (Monteith, 1981). Radiation
69 is thus a key driver of evapotranspiration which enters in most potential evapotranspiration
70 formulations (Fisher et al., 2011) and water balance models (Granier 1999; Ruffault et al.
71 2013; De Cáceres et al., 2015). Through its effect on leaf temperature and vapour pressure
72 deficit, radiation also influences the water status of the leaves which in turn will drive many
73 plant functions including growth, stomatal aperture and desiccation (Martin-StPaul et al.,
74 2023).

75 In regions with a complex orography, climatic variations can occur over distances ranging
76 from a few metres to a few kilometres. This phenomenon, referred to as topoclimate (Bramer
77 et al., 2018), can play a crucial role in shaping flora and fauna habitat as well as a multitude
78 of ecosystem processes related to climatic variability (Austin, 2002; Piedallu & Gégout,

79 2008; Randin et al., 2009). Accounting for topographic effects on spatial radiation patterns
80 has been well studied with the purpose, for instance, of improving niche models (that predict
81 the distribution of plants as a function of environmental variables) in mountainous areas
82 (Piedallu & Gégout, 2008; Randin et al., 2009). So far, such radiation data are measured or
83 computed from local meteorological stations, ~~or~~ from coarse-scale global meteorological
84 products such as reanalyses, or geostationary satellite data products at few kilometer
85 resolution (e.g. De Cáceres et al., 2018, Roerink et al. 2012).

86 Direct radiation is a primary driver of topoclimate variations, as it can undergo changes at a
87 very local scale due to several processes. At the scale of a massif, the surrounding
88 topography can cast shadows on a given point because the sun rays can be physically
89 interrupted. In other words, the presence of nearby high peaks will impact the rays directly
90 coming from the sun. At the scale of a point in space, the slope and aspect (azimuth), will in
91 addition modify the direct radiation intensity received. In the northern hemisphere, a south
92 face will receive more radiation than a north face, and this will be modulated by the angle
93 between the sun rays and the slope at the point. Similarly, the surrounding topography will
94 affect diffuse radiationluminosity (e.g., on cloudy days) isotropicallyanisotropically (at 360°),
95 leading to lower radiationluminosity in valley bottoms (*i.e.*, the skyview factor or the “bowl
96 effect”).

97 Historically, the primary method for accounting for the effects of topography on radiation has
98 been to rely on slope or aspect. Indeed, these parameters are relatively simple to measure
99 (e.g., through GIS) and the global radiation flux at the surface can be easily derived from
100 those (Austin et al., 1990; Carroll et al., 1999; Clark et al., 1999; Pierce et al., 2005).
101 However, this downscaling approach overlooks a significant portion of the processes
102 involved in radiation attenuation due to sky obstruction by surrounding topography. Shading
103 and the skyview were taken into account at a later stage, in particular in the radiation
104 parameterization scheme (Müller & Scherer, 2005) and in several of its applications (e.g.
105 Senkova et al., 2007; Buzzi, 2008). Regional climate models (RCMs), on the other hand,
106 calculate radiation by accounting for atmospheric processes in relation to land-surface
107 processes (energy balance etc...). Nevertheless, they typically operate on fixed grids,
108 usually at scales of several kilometres (Bailey et al., 2023), which is not precise enough for
109 operational use at point level. More recently, another method employed is statistical
110 downscaling, which is empirical and based on regressions (Davy & Kusch, 2021; Fealy &
111 Sweeney, 2008) or machine learning techniques (Hernanz et al., 2023). However, this
112 requires a lot of field data in different contexts to elaborate an empirical model.

113 Piedallu & Gégout (2008) proposed one method using the slope and the aspect of the point
114 to compute the sun intensity and taking into account the surrounding topography to compute
115 radiation accounting for direct shadowing. They produced a fine scale map (50 * 50 m) over
116 France which is dedicated to statistical niche modelling or mortality risk assessment
117 (Piedallu & Gégout, 2008). However, in the case of process-based vegetation models this
118 has several limitations. Firstly, their approach relies on interpolated meteorological station
119 data to compute the radiation correction at a monthly time step and is thus limited in terms of
120 temporal and spatial accuracy, leading to significant biases in vegetation growth or the
121 smoothing of climatic extremes. Secondly, they do not separate diffuse and direct radiation
122 using clouds but only use an empirical correction of the total radiation using cloud cover.
123 Finally, the skyview factor ~~“bowl-effect”~~ on diffuse radiation is not taken into account. This
124 method based on measurements is thus limited for projection purposes and requires a large
125 network of equipped stations, resulting in uncertainty. Moreover, it has been applied only to
126 France and has not been generalised to other regions or periods.

127 In this study we present a process-based method to downscale coarse resolution (0.1° at
128 best in general for reanalysis or meteorological models) or geostationary products (2 km
129 resolution at best) → global radiation data (such as global reanalysis or climate projections)
130 made on flat surfaces down to the level of 1 km to 30 m resolution Digital Elevation Model
131 (DEM) by accounting for slope, aspect, ~~and~~ the shadowing effect on direct radiation and for
132 the skyview factor ~~bowl-effect~~ on diffuse radiation. The method can be applied at any
133 resolution, depending on the choice of the DEM. Moreover, it can be applied to ~~relies on~~ any
134 type of radiation data, making it applicable to any region in the world and to historical periods
135 as well as future projections. The possibility to use reanalyses-derived radiation
136 ~~further~~ furthermore ensures physical consistency between the different climate variables
137 used in process-based models. The algorithm was tested on ~~the~~ Mont Ventoux and
138 compared with PAR measurements recorded during 2 years at 7 sites on this complex
139 topographic area. Finally we evaluated how this new radiation product can impact ecological
140 predictions ~~patterns~~ by simulating the gross primary productivity (GPP) and the risk of
141 drought-induced mortality for the European beech (*Fagus sylvatica*) ~~hydraulic failure for~~
142 *Fagus sylvatica* using two process-based models.

143 2. METHODS

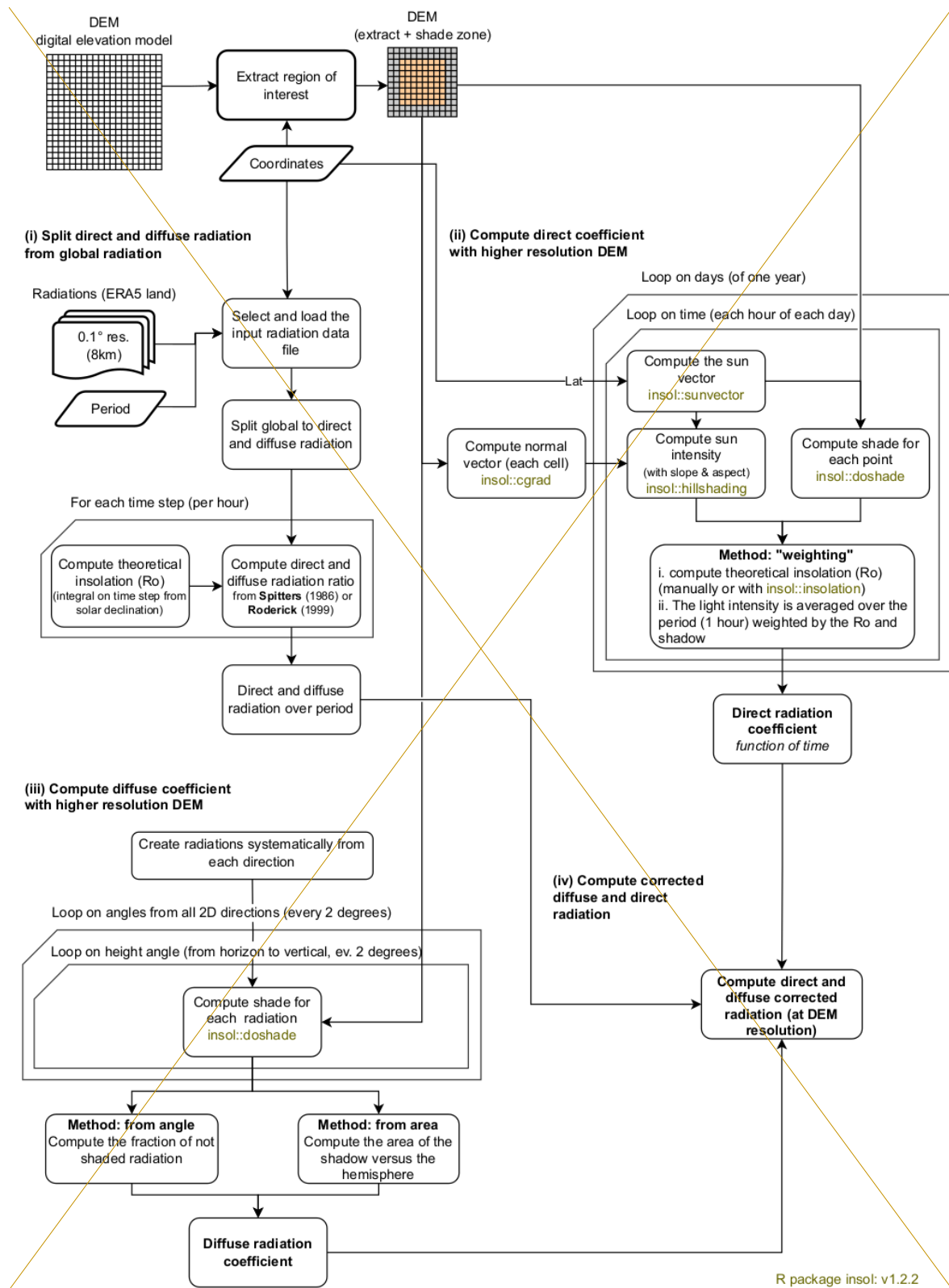
144 2.1. Radiation downscaling model

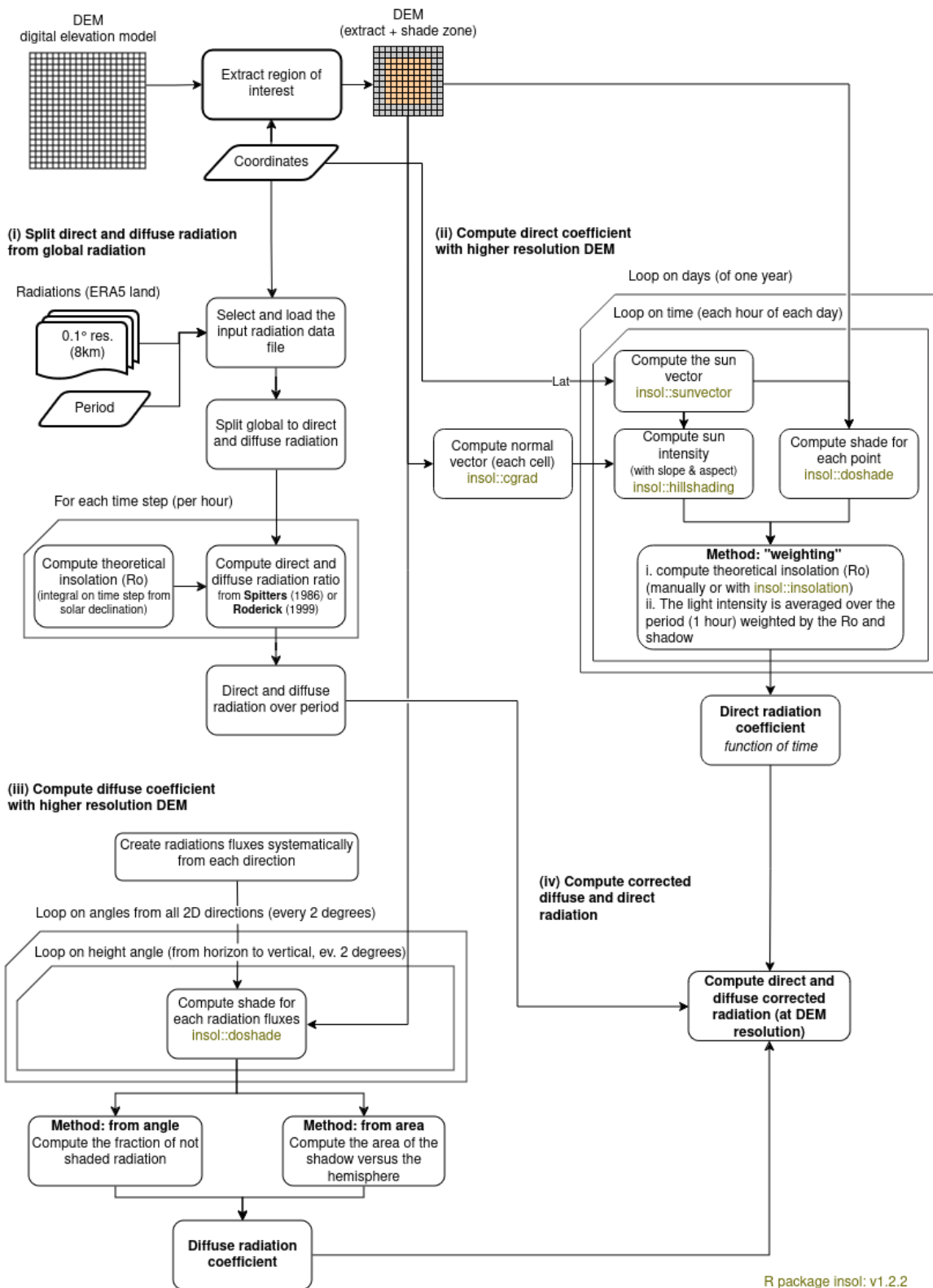
145 The proposed radiation downscaling model aims to refine sub-daily global radiation data
146 obtained from reanalysis at large scales to the resolution of a given DEM. This process-

147 based method can be adapted depending on the input dataset and accounts for the
148 shadowing effect on direct radiation and the skyview factor~~bowl-effect~~ on diffuse radiation. In
149 order to ensure its versatility and applicability, we reduced the need for external data that
150 can be challenging to obtain at the local scale, such as cloudiness (Dubayah and Loechel,
151 1997; Piedallu and Gégout, 2007). The only required input is a DEM whose resolution will
152 determine the~~must match the desired~~ final spatial resolution of the radiation data.

153 Our methodology involves four distinct steps, outlined as follows (see Fig. 1 for
154 visualisation):

- 155 i. Splitting direct and diffuse radiation from a large-scale global radiation dataset (optional if
156 the data already contain direct and diffuse radiation).
 - 157 ii. Downscaling direct radiation by considering local topography and shadowing effects.
 - 158 iii. Downscaling diffuse radiation by estimating the proportion of diffuse radiation that
159 reaches the target point relative to the surrounding topography.
 - 160 iv. Summing the downscaled direct and diffuse radiation components.
- 161 These steps are described in detail in the subsequent sections.





162 **Figure 1: Simplified workflow of radiation downscaling, showing the four different**
 163 **steps of the procedure. The bold boxes at the top left show the data required as**
 164 **inputs (DEM, coordinates, period and large scale radiation), the green boxes show the**
 165 **functions of the external R package used (insol), the truncated boxes show the loops**
 166 **and the rounded boxes show the various stages.**

167

2.1.1. Splitting direct and diffuse radiation

168 In cases where only global radiation is available from the input dataset, as in products like
 169 ERA5-Land (Muñoz-Sabater et al., 2021), a first step involves extracting hourly direct and
 170 diffuse radiation (Fig. 1.i). Various methods exist for this purpose (Oliphant & Stoy, 2018). In
 171 this study, we adopted the approach proposed by Spitters et al. (1986). This choice was
 172 driven by the relative simplicity of this approach and the fact that it was originally developed
 173 for European landscapes. Additionally, we explored other methods, such as the one
 174 proposed by Roderick (1999) and the one proposed by Bird and Hulstrom (1981). Results
 175 obtained using the Roderick (1999) method align consistently with those presented herein
 176 (results not displayed). Unlike the method by Spitters et al. (1986), the method by Bird and
 177 Hulstrom (1981) does not rely on global radiation values but instead aims to derive the
 178 values of direct and diffuse radiation from theoretical radiation, temperature, humidity,
 179 among other factors. However, the outcomes generated by this model significantly deviated
 180 from those obtained using the Spitters et al. (1986) method and exhibited inconsistency with
 181 available measurements (not shown).

182 The method of Spitters et al. (1986) that was used in this study is an empirical computation
 183 technique based on the ratio between theoretical extraterrestrial irradiance (R_0) and the
 184 observed value of global radiation (R_g). Specifically, it operates on the assumption that as
 185 the ratio of R_g to R_0 decreases, the proportion of diffuse radiation (R_{diff}) relative to direct
 186 radiation (R_{dir}) increases - an effect attributed to cloud cover.

187 To compute R_0 (in $WJ.m^{-2}.s^{-1}$), a common physically-based approach involves using the
 188 radiation incident on a plane parallel to the Earth's surface and the sine of solar elevation
 189 (which is dependent on latitude and solar time), as follows [\(Spitters et al., 1986; Widén &](#)
 190 [Munkhammar, 2019\)](#):

$$\begin{aligned}
 & \text{a. } R_0 = R_{sc} \left[1 + 0.033 \times \cos \left(\text{doy} \times 360 / 365 \right) \right] \times \sin(\beta) \\
 & \text{b. } \sin(\beta) = \sin(\lambda) \times \sin(\delta) + \cos(\lambda) \times \cos(\delta) \times \cos(15 \times (t_h - 12)) \quad (1) \\
 & \text{c. } \delta = \frac{\pi \times 23.45}{180} \times \sin \left(2 \times \pi \times \frac{\text{doy} + 284}{365} \right)
 \end{aligned}$$

192 With R_{sc} representing the solar constant (1 [361 W370-J.m⁻², Coddington et al., 2016.s⁻¹;](#)
 193 [I.E.A., 1978](#)), doy the day of the year, $\sin(\beta)$ the sine of the solar elevation angle, λ the
 194 latitude of the site (in radian), δ the solar declination angle (in degrees) [approximated using](#)
 195 [the Fletcher method as described in Eq. \(1.e\)](#) and t_h the hour (in solar time).

196 It's important to note that in this study, global radiation is not treated as a singular value but
 197 rather as an [averageaccumulation](#) over a short period of time (e.g., between h_t and h_{t+1} ,

198 using an hourly time step with ERA5-Land). Thus, $\sin(\beta)$ needs to be integrated:

$$199 \int_{h_t}^{h_{t+1}} \sin(\beta) = \sin(\lambda) \times \sin(\delta) + \cos(\lambda) \times \cos(\delta) \times \frac{15 \times \pi}{180} \times \left[\sin\left(\frac{\pi}{180} \times 15 \times (h_{t+1} - 12)\right) - \sin\left(\frac{\pi}{180} \times 15 \times (h_t - 12)\right) \right] \quad (2)$$

200 Then, we used the relationship between the fraction of diffuse radiation (R_{diff}) compared to
 201 global radiation data (R_g) and the fraction of global radiation data (R_g) compared to
 202 theoretical radiation (R_0), as recommended by de Jon (1980) [for hourly radiation](#) (described
 203 in Spitters et al., 1986, [including values for daily radiation](#)):

$$204 \frac{R_{diff}}{R_g} = 1 \quad \text{for} \quad \frac{R_g}{R_0} \leq 0.22$$

$$205 \frac{R_{diff}}{R_g} = 1 - 6.4 \times \left(\frac{R_g}{R_0} - 0.22 \right)^2 \quad \text{for} \quad 0.22 < \frac{R_g}{R_0} \leq 0.35 \quad (3)$$

$$206 \frac{R_{diff}}{R_g} = 1.47 - 1.66 \times \frac{R_g}{R_0} \quad \text{for} \quad 0.35 < \frac{R_g}{R_0} \leq K$$

$$207 \frac{R_{diff}}{R_g} = L \quad \text{for} \quad K < \frac{R_g}{R_0}$$

208 With $L = 0.847 - 1.61 \times \sin(\beta) + 1.04 \times \sin^2(\beta)$ and $K = \frac{1.47 - L}{1.66}$.

209 Following Spitters et al. (1986), the final step involves subtracting the circumsolar
 210 component (R_{circum}) of diffuse radiation from the direct flux: [Under clear skies, diffuse
 211 irradiance is anisotropic, due to the presence of aerosols in the atmosphere, and the
 212 intensity is therefore higher in the direction of the sun. It is thus necessary to attribute the
 213 excess diffuse irradiance observed near the direction of global radiation to direct radiation.](#)

$$214 R_{circum} = \cos^2\left(\frac{\pi}{2} - \beta\right) \times \cos^3(\beta) \quad (4)$$

215 To determine the corresponding fraction of diffuse radiation under intermediate sky
 216 conditions, [clear to cloudy skies](#), we adopt the interpolation method introduced by Klucher
 217 (1978):

$$218 \frac{R_{diff}}{R_g} = \frac{R_{diff}}{R_g} \div \left[1 + \left(1 - \left(\frac{R_{diff}}{R_g} \right)^2 \right) \times R_{circum} \right] \quad (5)$$

219 Finally, considering that global radiation (R_g) comprises [the sum of both](#) diffuse (R_{diff}) and
 220 direct (R_{dir}) radiation components, the value of R_{dir} can be directly inferred from the other two
 221 components.

222 **2.1.2. Downscaling direct radiation**

223 To downscale direct radiation (Fig. 1.ii.), two distinct processes were considered. Firstly, the
224 path of sun rays was examined to determine if any obstruction in the topography may block
225 them. Secondly, if unobstructed, the slope and aspect of the pixel are used to compute the
226 radiation intensity relative to a horizontal surface.

227 For both processes, the initial step involved computing the sun vector in three dimensions.
228 This was achieved using the R package "insol" (version 1.2.2, Corripio, 2020) and
229 specifically the "sunvector" function, which defines the vector based on longitude, latitude,
230 and time (day, hour, minute). To assess whether radiation is obstructed by a summit, the
231 close topography derived from a DEM is computed using the "doshade" function within the
232 "insol" package. To determine sun intensity, the "hillshading" function from the same
233 package is utilised, requiring both the sun vector and the topography (previously normalised
234 into unit vectors using the "cgrad" function). Note that the same package is now available for
235 python (on <https://pypi.org/project/insolation/> and <https://www.meteoexploration.com/insol/>).

236 Considering that the input radiation is accumulated over a specific period (e.g., 1 hour in
237 ERA5-Land), and to account for spatial variations in radiation intensity (primarily due to the
238 angle of the sun rays) and shadow projections, several time steps are employed for
239 downscaling the direct radiation. In this study, the default value of three time steps per hour
240 ($n = 3$) was adopted. Additionally, to aggregate the values while considering temporal
241 variations in radiation intensity, each value is weighted by the theoretical extraterrestrial
242 irradiance (R_0 in Eq. (1)). This yields a corrected direct radiation (R_{dir_cor}):

$$243 \quad R_{dir_cor} = R_{dir} \times \frac{\sum_{t_1}^{t_n} \left(R_0 \times S \times \frac{I_{slope}}{I_{vert}} \right)}{\sum_{t_1}^{t_n} R_0} \quad (6)$$

244 Where S represents the shadow parameter (with a value of 0 indicating shadow and 1
245 indicating no shadow), and I_{slope} and I_{vert} denote the illumination intensity over the slope and a
246 vertical surface, respectively, to derive the relative intensity of sunlight over the slope.

247 **2.1.3. Downscaling diffuse radiation**

248 Diffuse radiation is independent of the sun's inclination. It emanates uniformly from all
249 directions within the skydome, limited in this study to the top half-sphere. Therefore, its
250 downscaling (Fig. 1.iii) relies on the surrounding topography in all 360° horizontal
251 directions surrounding topography, particularly the proportion of diffuse radiation from all
252 directions that can reach the point under study.

253 Various methods exist to compute this fraction, including employing numerous random rays

254 or determining, for regular 3D distributed vectors, the level of shadow. In this study, a
255 specific method was devised. It involves computing, for each azimuth angle (with fixed steps
256 of 2°), the minimum unshaded radiation using the "doshade" R function described previously
257 and a DEM.

258 Subsequently, these values are utilised to calculate the shaded area of the top half-sphere
259 and thus the proportion of diffuse radiation reaching the focal point. Finally, this proportion is
260 applied to the diffuse radiation computed in Sect. 2.1.1 to derive the corrected diffuse
261 radiation (R_{diff_cor}).

262 The corrected diffuse and direct radiation can then be directly employed or recombined into
263 corrected global radiation (R_{g_corr}), e.g., to serve as input to a model of forest function or
264 dynamics.

265 **2.1.4. Digital elevation model data**

266 In various steps of the radiation downscaling, the utilisation of a DEM is imperative (Sect.
267 2.1.2 and 2.1.3). In this study, we evaluated radiation downscaling using different DEMs
268 characterised by varying resolutions.

269 The first dataset is the DEM provided by the Shuttle Radar Topography Mission (SRTM,
270 2013), offering a resolution of 1 arc-second (approximately 30 m). In order to clarify the
271 impact of using different resolutions, the resolution of the SRTM product was downgraded to
272 obtain products with resolutions of 60, 90, 125, 185, 250 and 500 metres using the
273 aggregate function (R, terra 1.7.23 library).

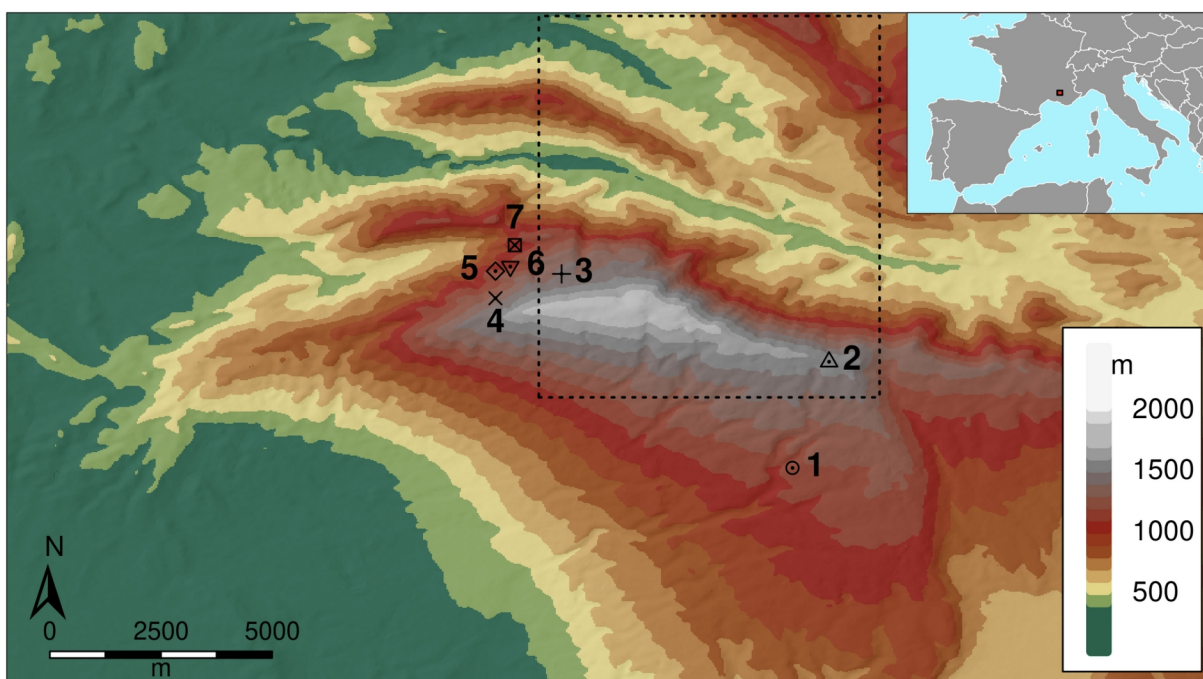
274 An additional series of DEMs was employed: the Global Multi-resolution Terrain Elevation
275 Data 2010 (GMTED2010, Danielson and Gesch, 2011), which encompasses spatial
276 resolutions of 30, 15, and 7.5 arc-seconds, corresponding approximately to resolutions of 1
277 km, 500 m, and 250 m, respectively. These datasets were compiled from diverse sources.
278 However, for the metropolitan France region, the primary source of the dataset was the 1
279 arc-second SRTM DEM.

280 The interest of these DEMs lies in their applicability beyond the geographic scope covered in
281 this study. Their availability at a global terrestrial scale renders them suitable for use in
282 various locations worldwide (with the exception of SRTM, which is limited to latitudes
283 between 60° north and 56° south).

284 **2.2. Study area**

285 The study area [was](#) Mont Ventoux, a mountain located in southeastern France, with its
286 highest point reaching an elevation of 1912 metres (44.174° N - 5.27794° E) (Fig. 2). While

287 Mont Ventoux is predominantly oriented in an east-west direction, it exhibits notable
 288 variations in slopes and aspectorientations. The southern flank is characterised by gradual
 289 inclines, whereas steeper slopes are evident on its northern side. Mont Ventoux presents a
 290 predominantly wooded landscape, featuring a mixed beech-fir forest on its northern side,
 291 and a mixed European beech-black pine forest on its southern side, particularly above an
 292 elevation of 800 metres (Jean et al., 2023). Below this elevation, the dominant species are
 293 more typical of the Mediterranean biome and include coppices of downy oak (*Quercus*
 294 *pubescens*), evergreen oak (*Quercus ilex*), Aleppo pine (*Pinus halepensis*)*Quercus*
 295 *pubescens*, *Quercus ilex*, *Pinus halepensis* as well as as natural regeneration of Atlas cedar
 296 (*Cedrus atlantica*)*Cedrus atlantica* from old plantation trials of the early 20th century.



297 **Figure 2: Map of the study area (Mont Ventoux). Mont Ventoux is located in**
 298 **southeastern France (see in the inset). Observation points (one symbol with**
 299 **associated number) and the ERA5-Land tile (in dotteddottle line) used in this study**
 300 **are indicated.**

301 **2.3. RGlobal radiation measurements**

302 On June, 27 2016, we installed seven mini-weather stations at different strategic elevations
 303 and locations on the north face of Mont Ventoux (Table 1), each equipped with loggers
 304 (YBdesign) and sensors for photosynthetically active radiation (PAR, 400-700 nm),
 305 temperature and relative humidity. The sensors were installed on a vertical pole and
 306 positioned horizontally (levelled with a spirit level). The PAR sensors (CBE80, brand
 307 Solems) and the thermo-hydrometers (EE07-PFT, brand E+E) were calibrated using a

308 reference weather station at the INRAE campus of Avignon before the beginning of the
 309 experiment. The mini-weather stations were positioned in clearings with forest edges
 310 extending beyond at a distance minimum of 30 m from the station. The data were recorded at
 311 one hour timestep. The photosynthetic flux density delivered by the sensors were converted
 312 into $W.m^{-2}$ of global radiation using an empirical relationship calibrated on the ICOS Font-
 313 Blanche experimental site (Moreno et al., 2021).

N°	Site	Latitude (°)	Longitude (°)	Elevation (m)	Slope (°)	Aspect(°)
1	Les Tournières	44.129646	5.320524	1159	5.5	250.1
2	Col de la fache	44.157819	5.331975	1575	6.2	201.2
3	Mont Serein	44.182886	5.257725	1413	4.0	234.1
4	dvx5	44.176758	5.238861	1320	20.8	347.2
5	Tc2	44.184014	5.239161	1116	33.1	351.0
6	dvx2	44.185142	5.243383	1074	28.0	355.1
7	142	44.190856	5.244869	1050	23.0	188.4

314 **Table 1. List and main characteristics of the observation sites in Mont Ventoux where**
 315 **radiation measurements were performed. Slope and aspect (azimuth) was computed**
 316 **from a 30 m resolution SRTM digital elevation model.**

317 The observed radiation wasis compared with the radiation from ERA5-Land before and after
 318 downscaling using DEMs at different resolutions. In order to facilitate the comparison
 319 between the ERA5-Land reanalysis dataset and observations, which may contain some
 320 gaps due to power failure, we aggregated radiation data over various periods (annually or
 321 seasonally). This approach involvedinvolves excluding time steps with missing data,
 322 separately for each site. Moreover, to compare with these observations, the correction of the
 323 light intensity due to the angle of the direct light rays in relation to the slope and
 324 aspectorientation (Sect. 2.1.2, the 'hillshading' function) was deactivated (in Sect. 3.1), as
 325 the measurements were carried out on a device placed horizontally.

326 **2.4. Modelling the effect of radiation downscaling on plant functions**

327 To quantify the influence of downscaled radiation on specific applications, we assessed the
 328 impact of radiation downscaling on beech (*Fagus sylvatica*) forest functioning using process-
 329 based vegetation modelling on the mountainous area of the Mont Ventoux massif (where
 330 radiation measurements were located).

331 We employed two complementary forest vegetation models to quantify how radiation

332 downscaling affects the spatial patterns of both Gross Primary Productivity (GPP) and
333 drought-induced risk of hydraulic failure. These models are, respectively, the forest growth
334 model CASTANEA (Dufrêne et al., 2005) and the plant hydraulic model SurEau (Cochard et
335 al., 2021; Ruffault et al., 2022).

336 CASTANEA is a comprehensive forest soil-vegetation-atmosphere model coupled with a
337 growth module. It simulates carbon (photosynthesis and respiration) and water fluxes
338 (transpiration, soil water content, soil water potential) at a half-hourly to daily time step for an
339 average tree in a homogeneous forest stand. A carbon allocation module assigns a
340 proportion of the daily Net Primary Productivity (NPP) toward various plant compartments
341 (stem, roots, fine roots, flowers, acorn, leaves, and storage) using empirical coefficients.
342 Carbon and water fluxes, including gross and net ecosystem photosynthesis, respiration,
343 transpiration, latent heat fluxes, soil water content, and plant water potential, have been
344 validated on different species and sites, including beech on Mont Ventoux (Davi et al., 2005;
345 Cailleret et al., 2011; Delpierre et al., 2012). In this study, the canopy Gross Primary
346 Productivity (GPP) was used to demonstrate the effects of radiation downscaling on potential
347 productivity.

348 SurEau is a plant-hydraulic model that is dedicated to simulate the risk of drought-induced
349 hydraulic failure due to xylem embolism, a leading mechanism of plant mortality under
350 drought (Cochard et al 2021; Ruffault et al 2022). The model simulates water fluxes and
351 simulates water fluxes and water potential through various compartments of the soil-plant
352 hydraulic continuum (Cochard et al 2021). At each time step (typically 30 minutes), the
353 model computes leaf stomatal and cuticular transpiration as the product between leaf-to-air
354 vapour pressure deficit (VPD) and stomatal and cuticular conductance. Then, stomatal and
355 cuticular fluxes are used to compute water potential along the soil-plant hydraulic continuum
356 at a half hourly time step, and considers leaf stomata and its regulation, and cuticular
357 transpiration plant organ capacitance anin the different plant compartments, while
358 accounting for the symplasmic capacitance and the hydraulic conductance losses due to
359 xylem embolism. Stomatal closure is regulated in a feedback manner based on leaf water
360 potential through empirical relationships (Klein, 2014; Martin-StPaul et al., 2017). Soil water
361 potential and hydraulic conductance are also computed from soil water content. The model
362 is parameterized with various measurable plant traits previously collected for the target
363 species (Ruffault et al., 2022). In this study, drought-induced risk of hydraulic
364 failureembolism (or the percentage loss of hydraulic conductance) in the vascular system
365 was used as a proxy for hydraulic risk during a given summer.

366 We conducted spatial simulations for one pixel at 0.1° resolution (~ 11 km * 8 km at these
367 coordinates), covering a large part of the Mont Ventoux northern face where the
368 measurements were conducted. The simulations covered the years 2016 and 2017,
369 encompassing the same geographical area as outlined in Sect. 2.3, spanning a segment of
370 Mont Ventoux ranging from 5.25° W to 5.35° W and from 44.15° N to 44.25° N.

371 Climate data were directly sourced from the ERA5-Land hourly dataset (Muñoz-Sabater et
372 al., 2021), including temperature, precipitation, wind speed, relative humidity, and global
373 radiation. The latter was downscaled using the method presented in Sect. 2.1, employing
374 one of the DEMs discussed in Sect. 2.1.4.

375 To maintain consistency and avoid introducing uncertainty from disparate datasets, all other
376 non-climatic inputs were set constant across the study area, as described hereafter. The
377 species selected, *Fagus sylvatica* (European beech), is one of the most common species
378 present on Mont Ventoux (Lander et al., 2021) and its traits are already available for the two
379 models (Cailleret & Davi, 2011; Cailleret et al., 2013-; Davi & Cailleret, 2017; Ruffault et al.,
380 2022), with a Leaf Area Index set at 3.5. The soil characteristic correspondedeorresponds to
381 the median value extracted from the whole studied area from the SoilGrids database (Poggio
382 et al., 2021).

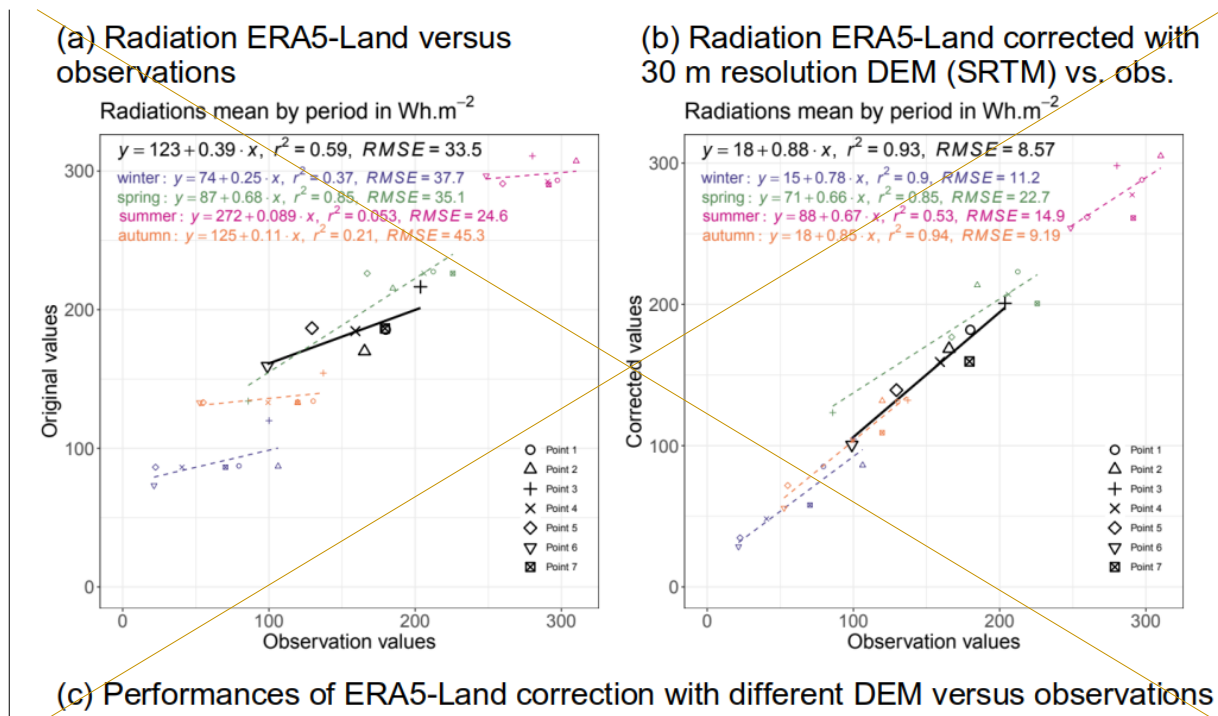
383 **3. RESULTS**

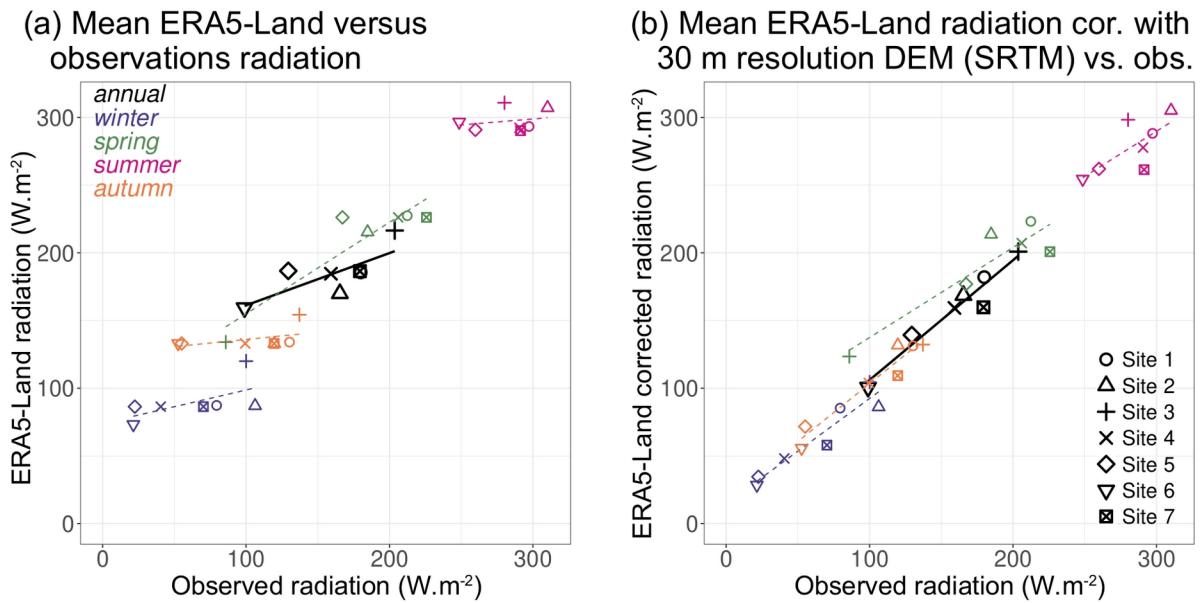
384 **3.1. Comparison between simulated and observed global radiation**

385 The comparison of ERA5-Land global radiation, both uncorrected and corrected, with
386 observed global radiation across the 7 studied sites showedshows the benefit of our
387 downscaling method in accurately estimating local global radiation (Figs. 3, 4 and Table
388 2Fig-3).

389 Specifically, the correlation between observed and simulated yearly mean global radiation
390 increasedincreases from $r^2 = 0.59$ to $r^2 = 0.93$, while the RMSE decreaseddecreases from
391 33.5 to 8.6 W.m⁻²Wh.m², for the raw ERA5-Land radiation and ERA5-Land radiation corrected
392 with a 30 m resolution DEM, respectively (Fig. 3 and Table 2Figs-3a and-3b). However, this
393 increase in the performance of estimating global radiation diddoes not progress consistently
394 as the resolution of our downscaling approach increases. We observedobserve a slight and
395 heterogeneous improvement in the corrected radiation from 1 km to 250 m resolution
396 compared to the raw ERA5-Land resolution (around 9 km). It is not until the resolution
397 reaches around 200 metres that a significant and continuous improvement wasis observed
398 (decrease in RMSE, increase in r^2) until 30 m resolution (Fig. 43-e).

399 Our results further showed that the absolute performance of radiation models (in terms of r^2)
 400 and their relative differences remained consistent across the different studied seasons (Fig.
 401 3a and 3b Table 2), despite some particularities. During winter, ERA5-Land raw data
 402 showed weak relationship correlation with observations (r^2 at 0.37 and RMSE at 38 Wh.m^{-2}),
 403 which substantially improved with correction ($r^2 = 0.90$, $\text{RMSE} = 11 \text{ Wh.m}^{-2}$). Similarly, but
 404 more pronounced, in autumn correlations and RMSE were considerably enhanced
 405 (respectively r^2 from 0.21 to 0.914 and RMSE from 45 to 9 Wh.m^{-2}). In summer, the
 406 correlation was almost zero with the ERA5-Land data, whereas it exceeded 0.5 with the
 407 corrected radiations. In contrast, the correlation was stable and high (0.85) in spring but did
 408 not improve with downscaling high (at 0.85), while RMSE is improved with correction (325 to
 409 23 Wh.m^{-2}). Further analysis also revealed that, the uncorrected (Fig. 3.a) and corrected
 410 (Fig. 3.b) seasonal data showed different behavior and so contrary to Fig. 3 (a), the
 411 equations of the seasonal curves for corrected ERA5-Land radiation closely aligned with the
 412 1/1 line, in accordance with an important decrease in RMSE (Fig. 3 b). It is noteworthy that
 413 most of the improvement comes from points located on northern slopes (points 4, 5 and
 414 6, Fig. 3). Accordingly, the daily bias from those points was reduced compared to
 415 uncorrected data, while points located on flat surfaces or southern slopes showed low and
 416 not significant similar limited bias (not shown).

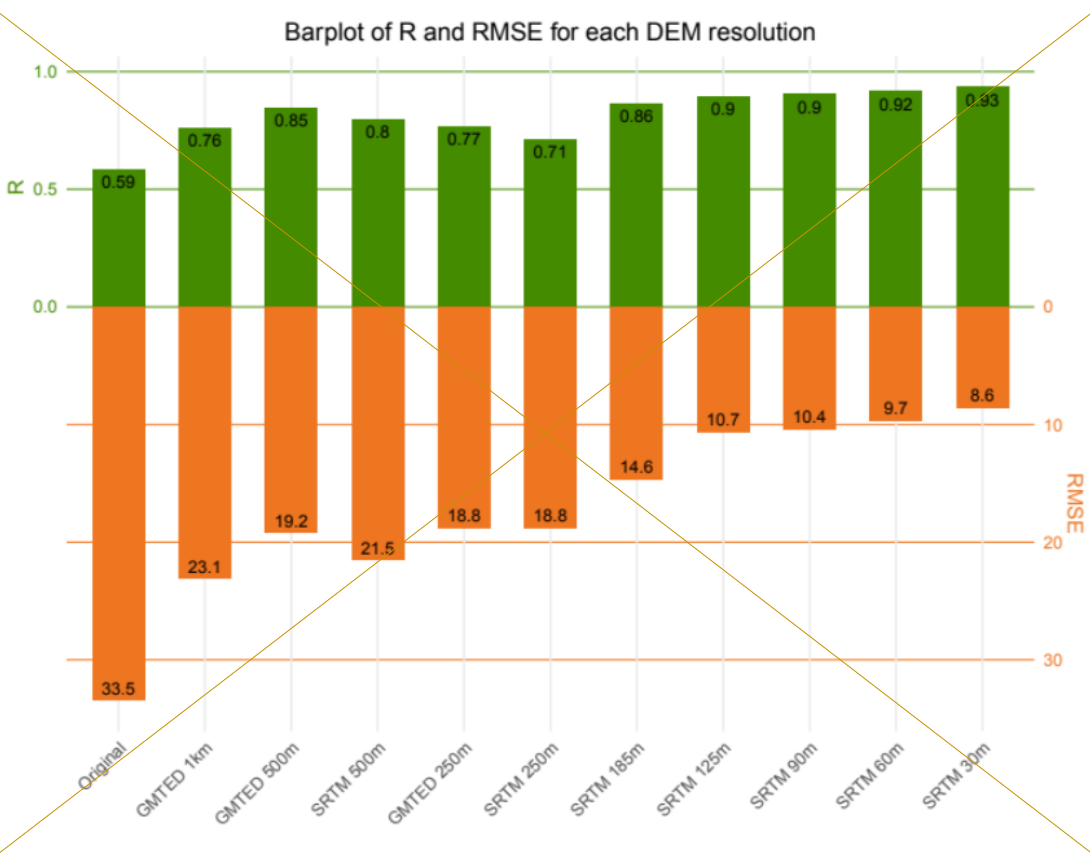
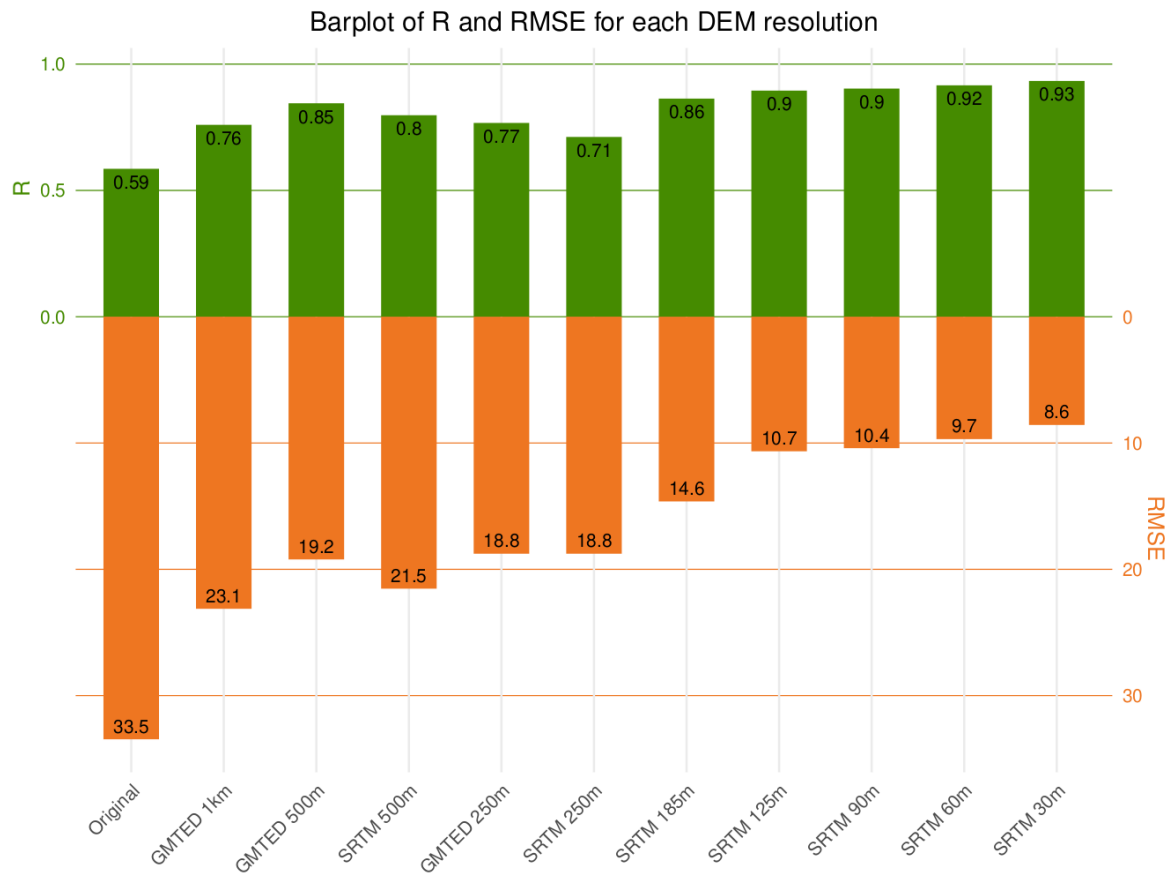




417 **Figure 3: Comparison of the observed radiation with the ERA5-Land product (a) and**
 418 **with corrected radiation from ERA5-Land using 30 m resolution different DEMs. (a)**
 419 **and (b). For each of the 7 points studied, the annual (in black) and seasonal (in**
 420 **colours) mean radiation ($W.m^{-2}$) are shown, as well as the linear regression line**
 421 **(equation, r^2 and RMSE, see table 2).represent the annual and seasonal correlation r^2**
 422 **and RMSE ($Wh.m^{-2}$) for each point. (c) shows the annual r^2 and RMSE (in black in (a)**
 423 **and (b)), for the original ERA5-Land data and each of the corrections obtained with**
 424 **the different DEMs**

	ERA5-Land vs. observations			ERA5-Land corrected with 30 m resolution DEM vs. obs.		
	equation	r^2	RMSE	equation	r^2	RMSE
annual	$y = 123 + 0.39 x$	0.59	33.5	$y = 18 + 0.89 x$	0.93	8.6
winter	$y = 74 + 0.25 x$	0.37	37.7	$y = 15 + 0.78 x$	0.90	11.1
spring	$y = 87 + 0.68 x$	0.85	35.1	$y = 71 + 0.67 x$	0.85	22.7
summer	$y = 272 + 0.09 x$	0.05	24.6	$y = 90 + 0.67 x$	0.53	14.8
autumn	$y = 125 + 0.11 x$	0.21	45.3	$y = 18 + 0.86 x$	0.94	9.1

425 **Table 2. Linear regression parameters and statistics (r^2 and RMSE, $W.m^{-2}$) for**
 426 **comparison of the observed radiation with the ERA5-Land product and with corrected**
 427 **radiation from ERA5-Land using 30 m DEM (see Fig. 3).**



428 **Figure 43: Comparison of the performances of observed radiation with the ERA5-Land**
 429 **product and with-corrected radiation from ERA5-Land using different DEMs with**

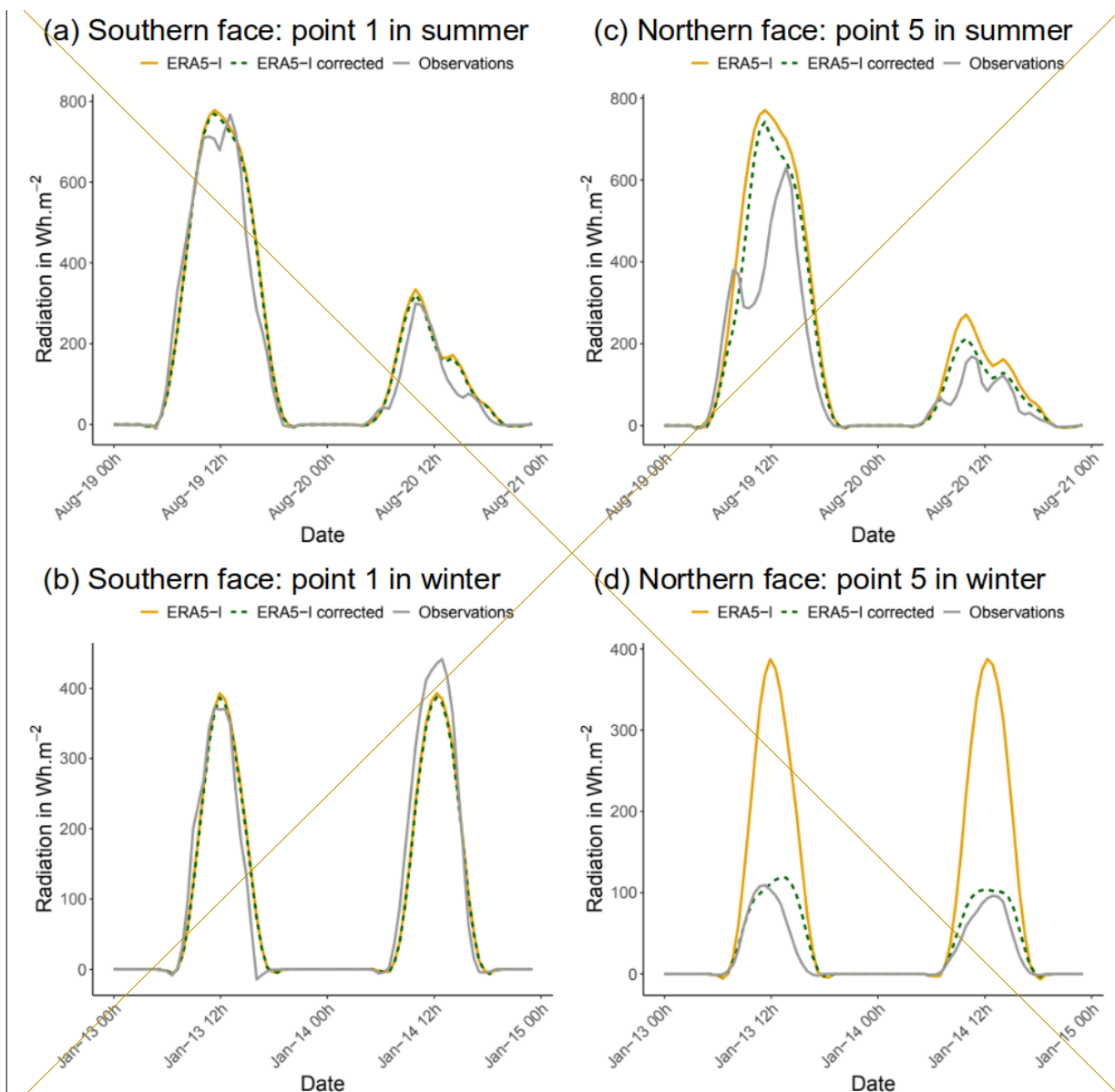
430 observed radiation. The annual ~~-(a) and (b) represent the annual and seasonal~~
431 correlation r^2 is represented in green and the RMSE ($W.m^{-2}$) in orange, and RMSE
432 ($Wh.m^{-2}$) for each point. ~~(c) shows the annual r^2 and RMSE (in black in (a) and (b)), for~~
433 the original ERA5-Land data and each of the corrections obtained with the different
434 DEMs

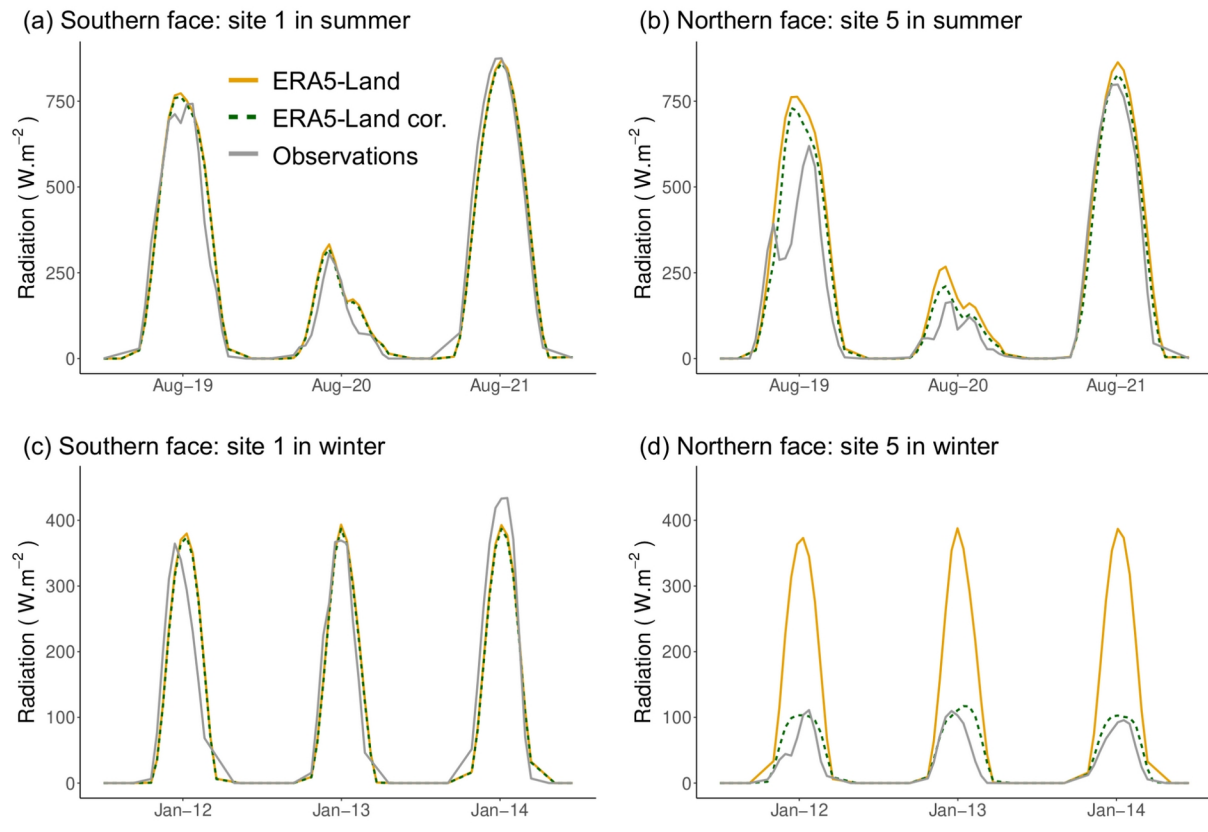
435 Figure 54 depicts the global radiation values for two distinct sites during two different
436 periods. Site 1 (refer to Table 1) represents a slightly south-facing location with little shade
437 from topographical features, particularly evident in winter. Site 5, on the other hand, is
438 situated on a north-facing slope (slightly west-facing) affecting sunlight exposure, especially
439 during winter months. Two ~~threetwo~~-day periods were selected for analysis: one in summer
440 (19-21 ~~and 20~~ August 2016) to observe the impact during peak sun exposure (on the 21st,
441 a cloudy and a rainy day (the 2020 August), and an intermediate day (the 19); and another in
442 winter (12 to 13 and 14 January 2017, cloudless days) to assess the effect of the
443 downscaling on low-inclination radiation in a mountainous region. Three types of radiation
444 values are presented: observed values (Sect. 2.3), original ERA5-Land values (9 km
445 resolution, tile indicated on Fig. 2), and values following the application of the radiation
446 downscaling with the SRTM DEM (~30 m resolution) (as described in Sect. 2.1, but without
447 “hillshading” function to be comparable with measurements which are made with sensors set
448 horizontal). The presence of clouds was assessed with data combining high-resolution cloud
449 information is directly inferred from satellite observations, such as the Copernicus
450 Atmosphere Monitoring Service (CAMS) solar radiation time-series data (available on
451 <https://ads.atmosphere.copernicus.eu/stac-browser/collections/cams-solar-radiation->
452 timeseries, last access the 22/10/2024), and are represented on Fig. S1. The difference
453 between sky-view and all sky radiation indicates the presence of clouds.

454 At site 1 (Fig. 5.a-c4.a-b), where surrounding topographical features have minimal impact on
455 radiation, the values from ERA5-Land wereare close to the observations and there wasis no
456 significant change after radiation downscaling. These trends heldheld for both clear and
457 cloudy days, and for both winter and summer periods. At site 5, disparities between original
458 and corrected ERA5-Land values wereare more significant due to topographical influences
459 than at site 1. In summer (Fig. 5.b4.e), discrepancies existedexist between original and
460 corrected ERA5-Land values. Corrected values accurately depict the evolution measured,
461 especially the 21 August, and constantly more closely representedrepresent measured
462 values, but still struggledstruggle to replicate sub-daily variations. Particularly, a dip in the
463 curve around 10am appearedappears to be present on the 19both-days, possibly indicating
464 a shadow or the presence of localized clouds or fog, but not represented in the original and

465 ~~the corrected radiation~~corrected radiation. In winter (Fig. 54.d), downscaling markedly
 466 ~~impacted~~impacts radiation values, with corrected values nearly four times lower than ERA5-
 467 Land values at the northern site, closely aligning with observed values.

468 Note that if the effect of the slope and aspect on radiation intensity were activated in the
 469 ~~script~~orientation were activated, the effect of the light intensity could increase in would be to
 470 ~~potentially increase~~the corrected radiation on the south faces, mainly on clear days and in
 471 winter (e.g. +10 % for point 1). By contrast it could, and on the contrary to considerably
 472 reduce the corrected radiation on cloud-free daysday (e.g. by a factor two for ~~21~~19 August at
 473 point 5).





474 **Figure 54: Radiation of original ERA5-Land data in orange, after downscaling with the**
 475 **SRTM DEM (30 m resolution) in dotted dark green and the observations in grey, for**
 476 **site 1 (a and b) and site 5 (c and d) and for two different dates: one in summer (19-**
 477 **2120 August 2016 in a and c) and one in winter (12-14 January 2017 in b and d)**

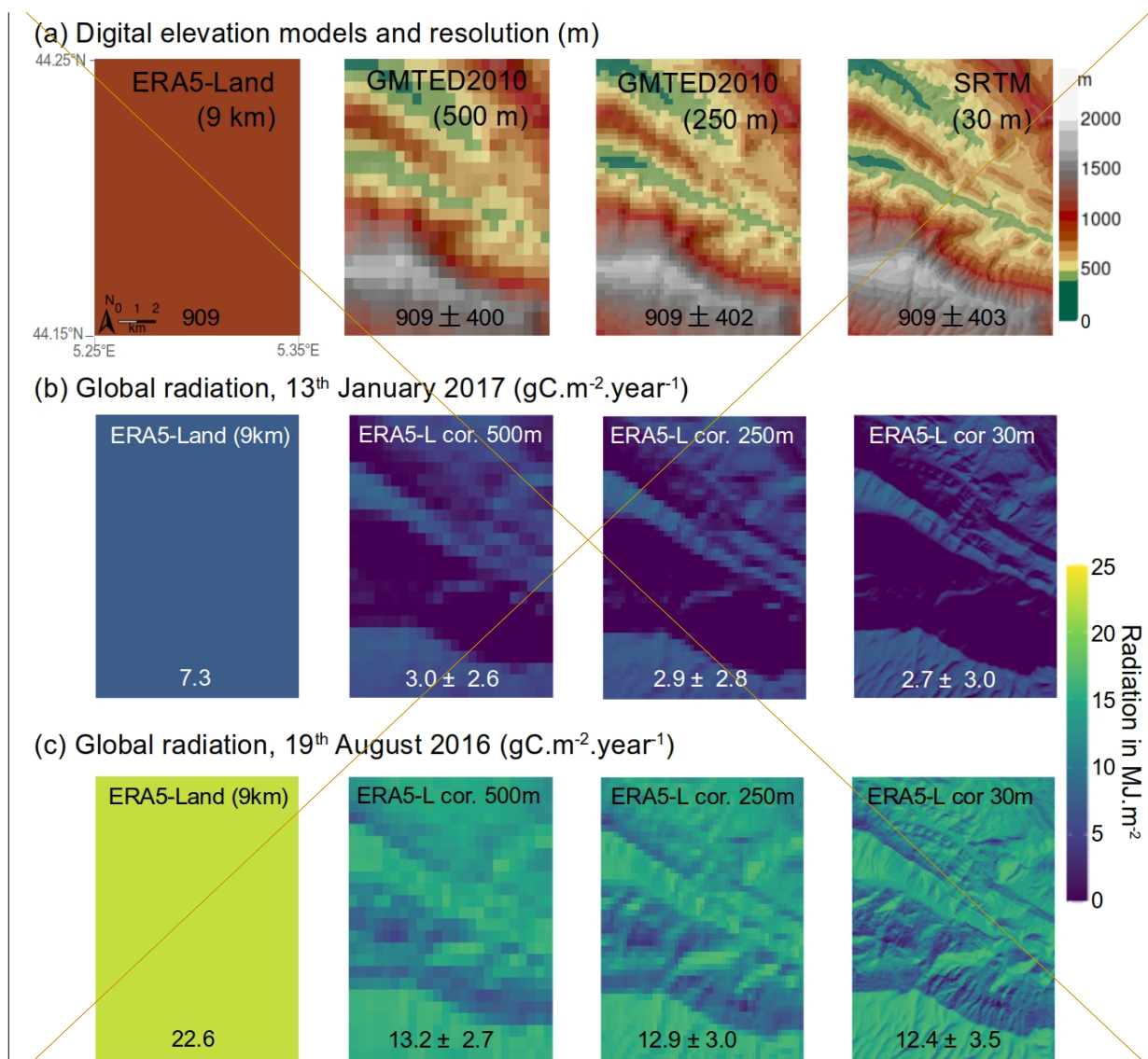
478 **3.2. Application on Mont Ventoux massif**

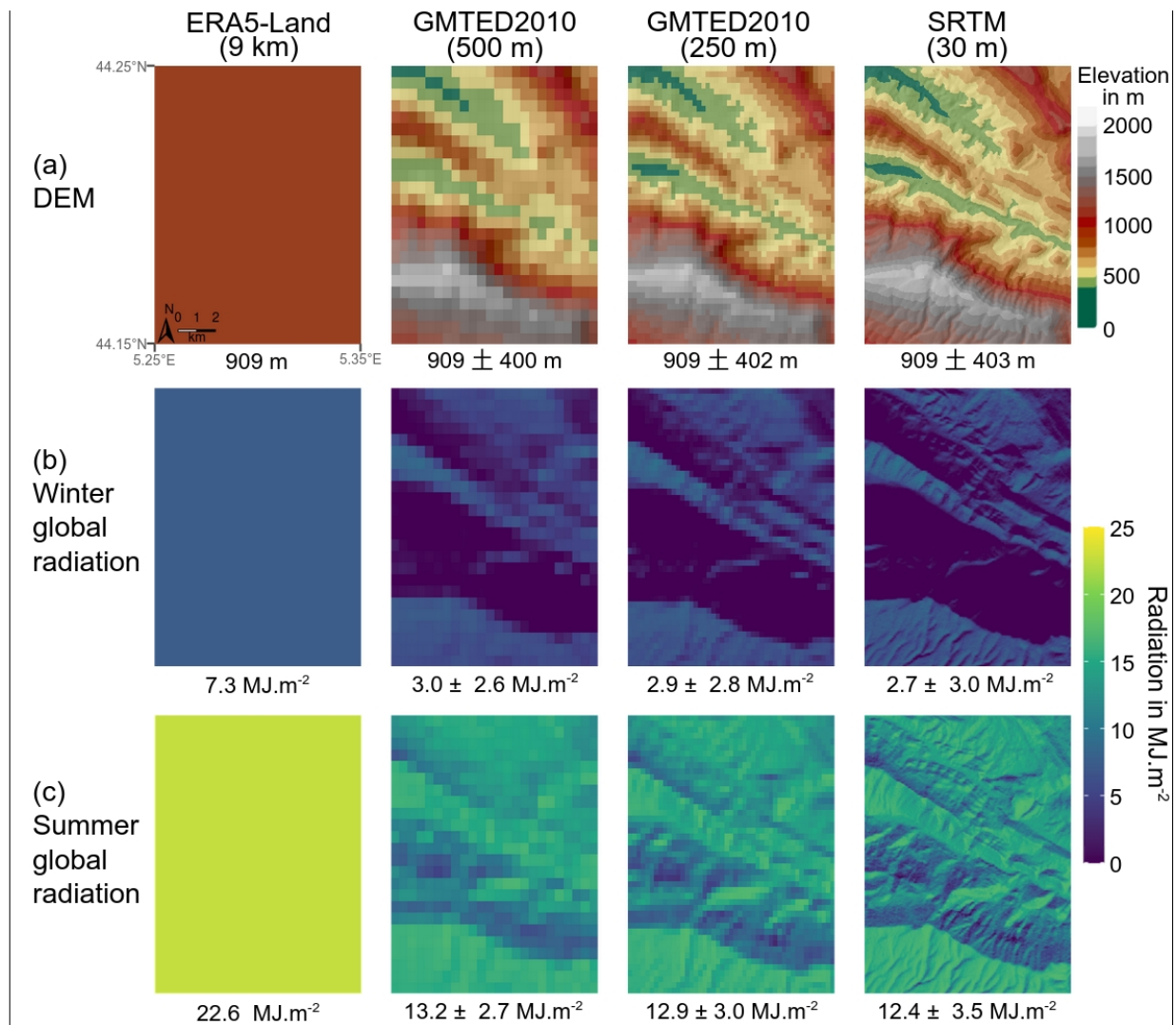
479 **3.2.1. Heterogeneity of global radiation**

480 Applying our approach across a heterogeneous geographical area illustrates the spatial and
 481 temporal variability in global radiation introduced by downscaling (Fig. 65).

482 Radiation downscaling ~~exerted~~exerts a clear impact in the mountainous region under study,
 483 halving original ERA5-Land global radiation. An evident differentiation ~~emerged~~emerges
 484 between south-facing slopes, which ~~received~~receive more radiation, and north-facing slopes,
 485 which ~~exhibited~~exhibit minimal radiation levels in winter (approaching zero). Mean radiation
 486 values ~~decreased~~decrease with increasing resolution of the three DEM used, indicating an
 487 average decrease of 10.7 % on 13 January 2017 and 5.9 % on 19 August 2016 when
 488 transitioning from the GMTED DEM at approximately 500 metres to the SRTM at
 489 approximately 30 metres resolution. Conversely, standard deviation ~~increased~~increases
 490 resolution, rising by 13.5 % and 30.0 %, respectively. ~~During~~ ~~However,~~ ~~during~~ winter, the
 491 standard deviation ~~was similar in mirrors the~~ magnitude of the mean due to low radiation
 492 values, whereas in summer, it ~~accounted~~accounts for 20 to 25 % of the mean.

493 These differences in standard deviation due to topography implied significant
 494 differences between the different DEMs, as well as with the original ERA5-Land values. For
 495 instance, the daily accumulation of maximum radiation value recorded on January 13th
 496 was 7.3 MJ.m⁻² in the reanalysis, whereas the maximum daily radiation reached it
 497 reaches 9.3 MJ.m⁻² in the ERA5-Land tile with downscaling conducted using the 250 m
 498 DEM. Similarly, on January 13th (Fig. 65.b), the spatial pattern representing a denser "line"
 499 denoting stronger radiation values around 5.3° E and 44.19° N was relatively narrow with
 500 the 30 m DEM (approximately 200 meters wide), whereas it doubled in width with the
 501 500 m DEM.





502 **Figure 65: Global radiation from ERA5-Land and resulting from downscaling obtained**
 503 **from different resolution DEMs. (a) ERA5-Land tile (left) and DEM resolution (500, 250,**
 504 **and 30 metres, from left to right). Daily global radiation for two distinct dates,**
 505 **(b) in winter (13 January 2017) and (c) in summer (19 August 2016). Regional mean**
 506 **values and standard deviations are indicated on the bottom of each map.**

507 **3.2.2. Modelling the influence of radiation downscaling on vegetation**
 508 **functioning**

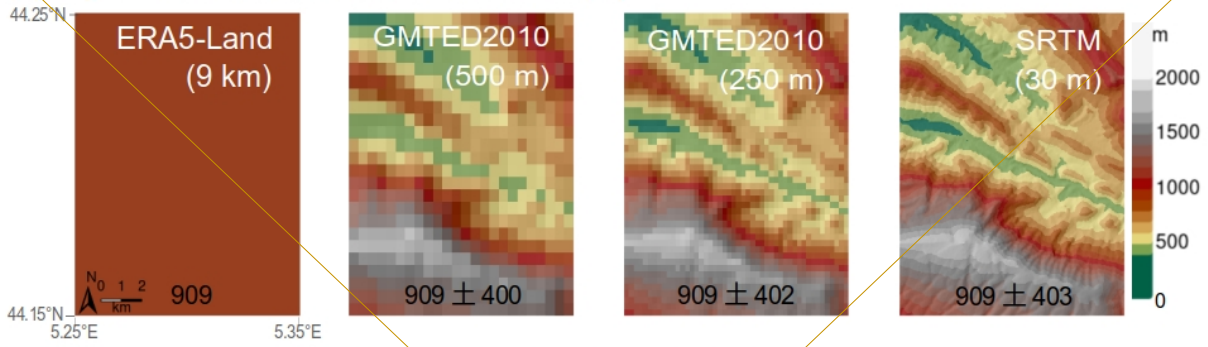
509 Modifying radiation across the entire area according to each DEM had a tangible impact
 510 on the predictions of vegetation processes as presented on models output as shown in Fig.
 511 76. In general, the simulations remained consistent across the studied area, despite
 512 potential variations introduced by the different topographies used during downscaling. With
 513 the three different downscaling (from 8 km to 500 m, 250 m and 30 m), downscaling, there is
 514 a discernible reduction in Gross Primary Productivity (GPP) ranging between 5 % and 8 %,

515 as well as in the risk of hydraulic failure, which decreases between 14 % and 23 %.
516 Moreover, the standard deviation introduced between the values wasis quite significant,
517 varying between 8 % and 13 % for the two outputs studied.

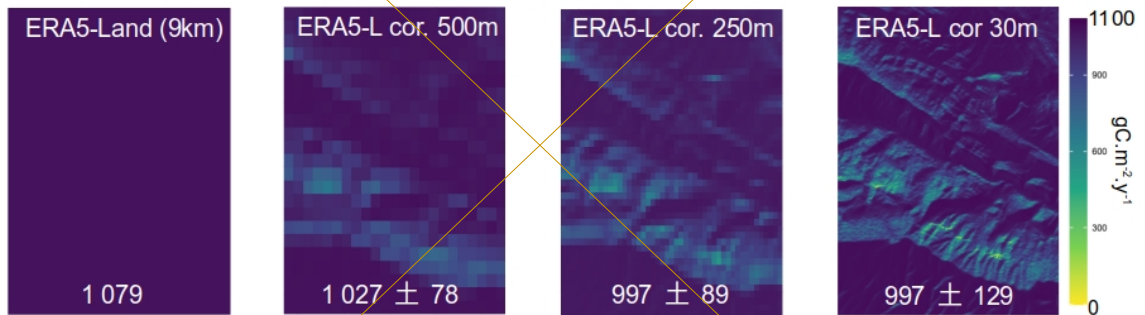
518 Upon comparing the patterns obtained with the corresponding DEMs, we observed it
519 ~~becomes evident~~ that south-facing slopes tended~~tend~~ to exhibit higher annual productivity
520 (Fig. 76.b) but were~~are~~ susceptible to greater hydraulic stress (as indicated by darker
521 colours in Fig. 76.c). Conversely, north-facing slopes generally manifested~~manifest~~ lower
522 GPP as simulated by the CASTANEA~~Castanea~~ model, yet exhibited~~exhibit~~ a reduced risk of
523 hydraulic failure.

524 To evaluate the potential impact of these discrepancies on drought-induced
525 mortality~~mortality risk~~, we computed the risk of hydraulic failure from the SurEau~~embolism~~
526 simulations. The relationship between mortality due to and embolism level water stress and
527 risk of hydraulic failure is often conceptualised as a threshold effect (Choat et al., 2018),
528 although this notion is occasionally questioned (Hammond et al., 2021). Setting at 50%
529 ~~the threshold at which mortality occurs to 50 % of~~ risk of hydraulic failure threshold at
530 which trees die, we obtained drought-induced ~~obtain~~ mortality percentages in term of surface
531 of 100 %, and 97 %, 98 % and 89 % for the original ERA5-Land tile, and the data
532 downscaled to 500 m, 250 m and 30 m, respectively. Given that the total soil available water
533 accessible for the trees useful reserve used in this study came~~comes~~ from a single value
534 taken from the median over the area of the SoilGrids database (Poggio et al., 2021), and
535 that this value is subject to uncertainty~~open to question~~, these results must be compared
536 relatively to each other.

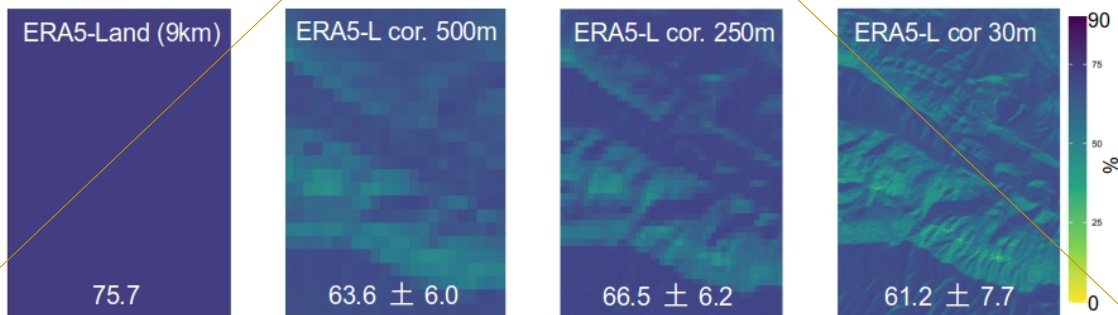
(a) Digital elevation models and resolution (m)

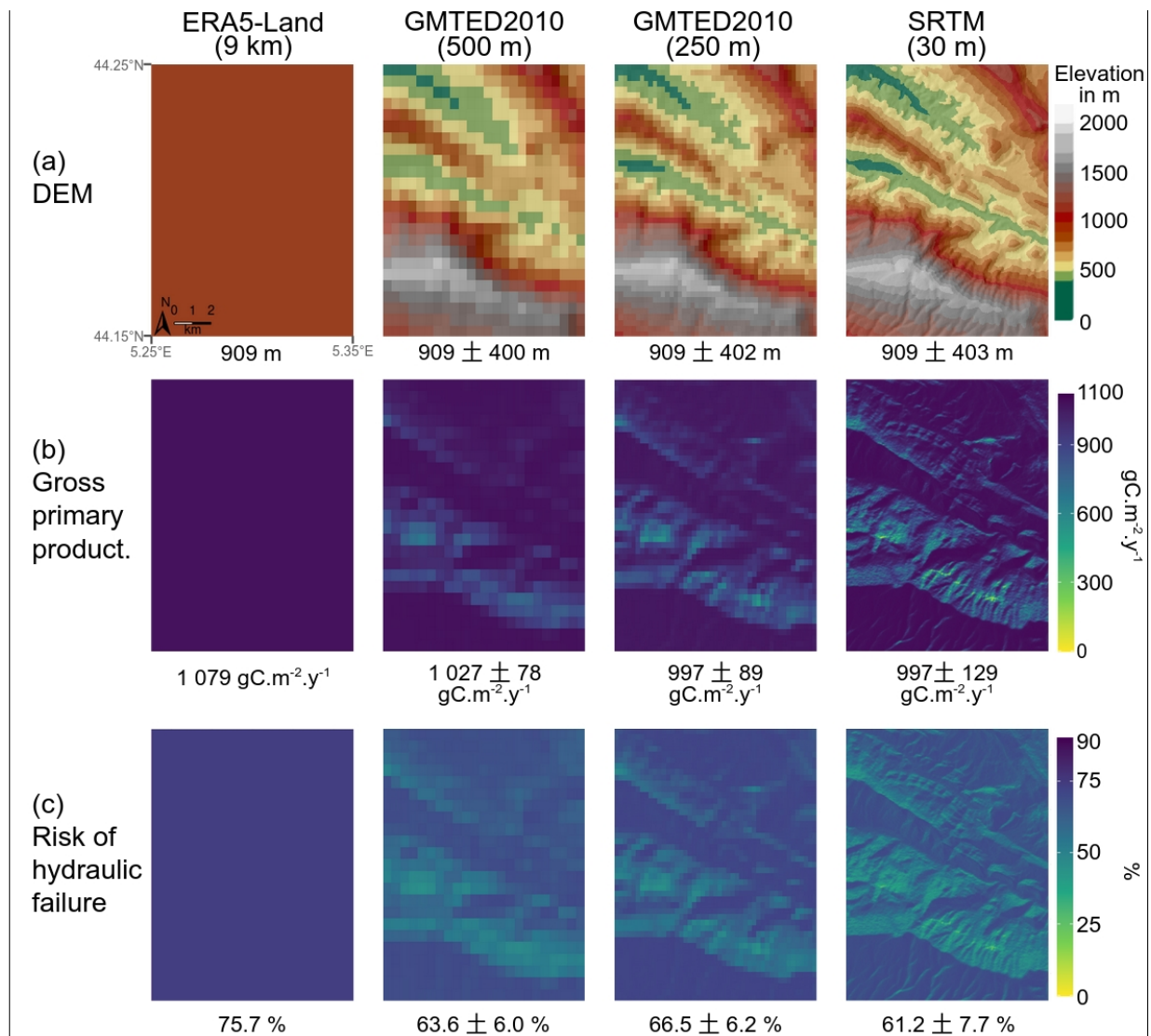


(b) Gross primary productivity (GPP, $\text{gC}\cdot\text{m}^{-2}\cdot\text{year}^{-1}$) with *Castanea*



(c) Risk of hydraulic failure (%) with SurEau





537 **Figure 76:** Gross primary productivity and risk of hydraulic failure simulated with, respectively, **CASTANEA** and SurEau, from ERA5-Land and resulting from
538 **respectively, CASTANEA** and SurEau, from ERA5-Land and resulting from
539 **global radiation downscaling obtained from different resolution DEMs. (a) ERA5-Land**
540 **tile (left) and DEM resolution (500, 250, and 30 metres, from left to right). (b) Gross**
541 **primary productivity simulated with CASTANEA. (c) Risk of hydraulic failure**
542 **simulated with SurEau. Regional mean values and standard deviations are indicated**
543 **on the bottom of each map.**

544 **4. DISCUSSION**

545 **4.1. Performance of the downscaling method**

546 The radiation downscaling method we present in this study significantly improved radiation
547 predictions in mountainous regions compared to those provided by reanalysis products.
548 More specifically, we demonstrated that accounting for the impact of topography and

549 distinguishing between direct and diffuse radiation allowed us to better capture seasonal
550 radiation patterns. On the north-facing side of our study area, where global radiation is
551 reduced due to the obstruction of direct sunlight by surrounding mountains, our downscaling
552 method significantly lowered radiation levels, particularly during winter when the Sun is at its
553 lowest position on the sky. Conversely, on the south-facing slopes, the steepness of the
554 terrain and the more direct alignment with the sun resulted in increased radiation levels. This
555 effect was also particularly pronounced in winter, when the Sun is lower in the sky but more
556 favourably oriented towards these slopes. Consequently, our method represented the spatial
557 heterogeneity of radiation that can be observed in complex terrain, significantly improving
558 radiation estimations from larger scale reanalysis products when a fine downscaling scale is
559 chosen. This corroborates the results reported by other studies based on slope, aspect ratio
560 and skyview, which indicate improved results after downscaling (Müller and Dieter, 2005;
561 Senkova et al., 2007; Buzzi, 2008). Nevertheless, none of these studies combines both high
562 spatial (here ~30 m) and temporal resolution (hourly). Furthermore, by comparing precisely
563 resolved data combining high-resolution cloud information is directly inferred from satellite
564 observations (Fig. S1), the quality of our results is confirmed. While in summer, the CAMS
565 data are consistent with both our results and the observations, in winter the results
566 presented in Fig. 5 are much closer to the observations at the south-facing site, while at the
567 north-facing site the topographical correction allows us to be very close to the observations,
568 whereas the CAMS data are very far from them.

569 Our analysis showed a clear but non-uniform improvement in radiation estimates as the
570 resolution of our downscaling method increased. While no continuous improvement was
571 observed at resolutions coarser than 250 m, a gradual improvement emerged for finer
572 resolutions, down to 30 m. This suggests that topoclimatic processes, such as the effects of
573 topography on local radiation patterns, operate at these finer spatial scales, highlighting the
574 importance of high-resolution estimations for accurately representing the influence of terrain
575 on local climate. On the other hand, our results for resolutions coarser than 250 m, suggest
576 that insufficient improvement in resolution during the downscaling introduces some variance
577 (due to the inherent uncertainty of the method and additional processing of the variable)
578 which can mitigate improvements in radiation representation at the site level.

579 The results of our study indicate that the radiation downscaling method developed in this
580 study effectively captures the overall trend of radiation distribution across mountainous
581 regions. The daily patterns are effectively represented, however sub-daily variations may not
582 fully account for microclimatic variations, especially considering the spatial heterogeneity
583 within a grid pixel at the resolution of climate data. This is the case for example with cloud
584 cover, which can be highly variable in mountainous regions.

585 As we clearly observed in our study area, the impact of radiation downscaling was primarily
586 observed in regions with significant shadow casting, whose effect becomes more
587 pronounced as the Sun's zenithal angle decreases. Due to energy equilibrium and
588 conservation at large scale, this implies that an increase in radiation was observed on south-
589 facing slopes or on mountaintops. This effect was particularly pronounced when the angle
590 between the incoming direct radiation and the aspect of the relief (slope and azimuth)
591 approaches perpendicularity relative to a flat surface. However, it's worth noting that our
592 study area is not characterised by extremely steep mountains, so these effects are primarily
593 observed on moderate slopes. In regions with much steeper terrain, we would expect the
594 impact of topography on radiation to be even more pronounced, especially in valley bottoms,
595 where shading effects could remain significant even on south-facing slopes.
596 ~~However, our findings suggest that, overall, radiation downscaling significantly reduces~~
597 ~~radiation levels on the north-facing side, particularly during winter, as a result of the~~
598 ~~obstruction of direct radiation by surrounding mountains. Conversely, this radiation decrease~~
599 ~~on north-facing slopes is compensated by an increase on south-facing slopes. Consequently~~
600 ~~our method improves methods already available to downscale radiation (Piedallu & Gégout,~~
601 ~~2008).~~

602 An important source of uncertainty in our radiation downscaling method likely stems from the
603 way global radiation is split into direct and diffuse components using the ratio of R_g to R_0 as a
604 proxy for cloud cover. This approach cannot capture the spatial and temporal heterogeneity
605 of cloud cover, which can be especially significant in mountainous regions (Buzzi, 2008).
606 This explains why, while daily patterns were effectively estimated, sub-daily variations were
607 more difficult to capture. For instance, in Figure 5.b, the dip around 10 a.m. the 19 August
608 may suggest the presence of microclimatic conditions, such as clouds or fog, an effect not
609 considered in our downscaling method. Actually, the original ERA5-Land data cannot depicts
610 the presence of isolated clouds as it happens on the day presented for summer in Figure 5
611 as they provide averaged values of incoming radiation over the whole mesh area. Such
612 occurrences could be tracked by using higher resolution solar radiation products such as
613 those obtained from satellite imagery and in particular geostationary satellites with a spatial
614 resolution in the order of 2 to 3 km and a time resolution between 5 and 15 minutes (ex.
615 Roerink et al. 2012, Bojanowski et al. 2014).Indeed, this dip may be associated with the
616 presence of small clouds or fog capping Mont Ventoux during morning, signalled by the
617 drop-out between the CAMS clear-sky and all sky (Fig. S1). Similarly, the small dip observed
618 shortly after in Figure 5.a is actually related to the presence of small clouds of fog capping
619 Mont Ventoux during morning, moving from one site to another. Further analyses with such

620 data could help quantify the extent to which this effect contributes to overall uncertainty of
621 our methodology.

622 ~~The results of our radiation downscaling method reveal a significant improvement of the~~
623 ~~representation of radiation from 9 km reanalysis, for all seasons, but especially on north-~~
624 ~~facing slopes and more pronounced in winter. The impact of radiation downscaling is~~
625 ~~therefore primarily observed in regions with significant shadow casting, and it becomes more~~
626 ~~pronounced with the sun's zenithal angle. This emphasises the necessity to correct the~~
627 ~~radiation to accurately depict the dynamics of radiation in mountainous regions.~~
628 ~~Nevertheless, the method has its limitations, as it is linked to the quality of DEM and does~~
629 ~~not take into account climatic heterogeneity, which can explain cloud cover on a smaller~~
630 ~~scale than the reanalysis data. Thus in Figure 4.c, the dip at around 10am may indicate the~~
631 ~~presence of micro-climatic conditions, such as fog, an effect that was not considered in our~~
632 ~~downscaling method.~~

633 ~~Additionally, our analysis revealed intriguing results concerning the impact of different DEM~~
634 ~~resolutions. While no clear improvement was observed with a resolution greater than 250 m,~~
635 ~~a clear gradual improvement appears for resolutions finer than 250 m (up to 30 m). This~~
636 ~~suggests that higher resolutions are crucial for effectively capturing the nuances of radiation~~
637 ~~dynamics. We hypothesise that insufficient improvement in resolution during the~~
638 ~~downscaling introduces some variance which is not adequately compensated by~~
639 ~~improvements in radiation representation at the site level.~~

640 **4.2. Implications of radiation downscaling for modelling studies and** 641 **perspectives of improvements**

642 Using downscaled radiation estimations as input in two process-based forest models
643 provides an overview of the impact that radiation downscaling can have on different forest
644 processes, namely Gross Primary Production (GPP) or drought-induced mortality. Overall,
645 our results revealed that the effects of topography on local radiation patterns can have
646 important implications on these key forest processes. For instance, when considering
647 processes that are based on thresholds, such as the drought-induced mortality associated
648 with risk of hydraulic failure, the mortality rate was reduced from 100 % to 89 %. As could be
649 deduced from the results on radiation alone, the impact of downscaling on GPP and drought-
650 induced mortality was most pronounced in areas with significant topographic features, such
651 as north-facing slopes due to shading or south-facing slopes due to increased radiation
652 levels.

653 While the effect of topography on forest ecological processes is often assessed through its

654 impact on temperature or precipitation patterns (Randin et al., 2009), these results suggest
655 that spatial heterogeneity of radiation, through its interaction with topography, seems also
656 crucial for accurately assessing ecological responses and potential threshold effects in
657 complex terrain. Future studies could benefit from integrating our radiation downscaling
658 method to improve predictions of forest functioning at a very local scale.

659 ~~The application of downscaling with the SurEau and CASTANEA models provides an~~
660 ~~overview of the impact that downscaling can have on different parameters, such as GPP or~~
661 ~~tree mortality risk due to hydraulic failure. Mont Ventoux was used as a benchmark site for~~
662 ~~testing applications. The impact of downscaling on these parameters is most pronounced in~~
663 ~~areas with significant topographic features, such as mountainous regions or canyons, with~~
664 ~~lower radiation levels on north-facing slopes due to shading and higher radiation levels on~~
665 ~~south-facing slopes due to sun intensity.~~

666 However, these findings should be interpreted with caution as, in our study, only solar
667 radiation was downscaled, leading to potential decoupling with the other forcing variables
668 (temperature, humidity, precipitation and wind). Downscaling methods exist for these
669 variables, for example the use of simple adiabatic gradient for temperature, or kriging
670 methods or high resolution radar data for rainfall (Liston and Elder 2006, Davy & Kusch,
671 2021) or dynamic models (Maraun et al., 2010), but they are not consistent with the one
672 proposed here. We therefore need to check the consistency of each of the downscaling
673 methods, or evaluate if it is possible to integrate this method or its outputs to downscale
674 other variables with other methods. Indeed, it is important to start from physically-consistent
675 data: in this case ERA5-Land, but which can be adapted, as the method can be adapted to
676 any global (or direct and indirect) radiation input. Finally, the method developed here is only
677 applicable to shortwave radiation, which is the only radiation currently required by the
678 models used. Nevertheless, the principle of the method presented here could be used as a
679 starting point for downscaling longwave radiation. Following the principle presented in
680 Senkova et al (2007), the method used for diffuse radiation (based on the skyview) could be
681 partially applicable to longwave radiation. If it is considered as isotropic, incoming
682 atmospheric radiation could be downscaled directly on the basis of the methodology used to
683 downscale diffuse incoming solar radiation. However, it would be necessary to account for
684 the radiation emitted by land surfaces in view as emitted radiation from the surface is usually
685 significantly higher than atmospheric radiation (this would be particularly true for cloudless
686 skies). This would require the knowledge of the surface temperatures of the surrounding
687 areas, but it is also important to recall that the net longwave radiation has a significantly
688 lower impact than the net shortwave radiation on the surface energy balance (ex. Mira et al.
689 2016).

690 ~~These findings have to be taken with caution as only radiation was downscaled making the~~
691 ~~other forcing variables (temperature, VPD, rainfall) decorrelated which partly limits the~~
692 ~~interpretation. However, with these limits in my mind and assuming impact models can be~~
693 ~~used to assess climate products in this context (Stephanon et al., 2015), it appears that~~
694 ~~radiation downscaling has profound implications on impact simulation (Fig. 6). In particular~~
695 ~~when considering processes that are based on threshold, such as the mortality risk~~
696 ~~associated with hydraulic failure, in our example, the mortality rate can go from 100 % to 89~~
697 ~~%. Thus, assessing the spatial heterogeneity of radiation, through its interaction with~~
698 ~~topography, seems crucial for accurately assessing ecological responses and potential~~
699 ~~threshold effects in complex terrain. Future studies could benefit from these methods to~~
700 ~~improve the prediction of species distribution or ecosystem functions at local level.~~

701 **5. CONCLUSION**

702 In this study, we developed a process-based method to downscale global radiation data
703 made on flat surfaces, such as coarse spatial resolution global reanalysis data. The method
704 builds upon existing research and goes further than traditional process-based radiation
705 downscaling methods, by accounting for the shadowing effect on direct radiation and for the
706 ~~skyview factor~~~~bowl-effect~~ on diffuse radiation (Piedallu & Gégout, 2008). The recent ERA5-
707 Land hourly data available at 9 km resolution was used to compare on ~~the~~ Mont Ventoux the
708 impact of radiation downscaling computed from different digital elevation models.

709 The radiation downscaling method effectively ~~capture~~~~captures~~ the overall trend of radiation
710 distribution across mountainous regions. ~~Agreement with observations was improved for~~
711 ~~downscaled radiation. Downscaled radiation is improved~~ compared to original ERA5-Land
712 data, especially during winter months, due to the higher zenithal angle. ~~This improvement~~
713 ~~was particularly significant and increased gradually. However, the improvement is significant~~
714 ~~only~~ after a certain spatial resolution (~ 150 m) ~~and gradually increases thereafter~~. The
715 implications of downscaling for modelling studies was further investigated using two different
716 process-based models representing gross primary productivity and risk of hydraulic failure.
717 The impact of downscaling on those ~~variables was~~ is most pronounced in areas with
718 significant topographic features, such as mountainous regions or canyons. Assessing the
719 spatial heterogeneity of radiation, through its interaction with topography, is crucial for
720 accurately addressing ecological responses and potential threshold effects in complex
721 terrain.

722 The method can be applied at any resolution, depending on the choice of the DEM.

723 Moreover, it ~~can be applied to~~ relies on any type of radiation data, making it applicable to any
724 region in the world and to historical periods as well as future projections. Finally, the method
725 could involve other types of climatic data from the same input dataset, such as temperature
726 or precipitation, thereby ensuring physical consistency between the variables. In the future
727 such methods could be included in more generic climate downscaling tools (e.g. Meteoland,
728 De Cáceres et al., 2018) to facilitate the application of process based models at fine
729 resolution.

730 **Code availability**

731 The scripts corresponding to the method developed in this article is available on GitLab at
732 https://forgemia.inra.fr/urfm/modeldata_toolkit (commit `afc05ed2`) with the prefix
733 “RadDownscaling”.

734 The SurEau model code presented in section 2.4 and whose results are presented in section
735 3.2 is available on GitLab at <https://forgemia.inra.fr/urfm/sureau> (commit `ca19abfb`), while the
736 CASTANEA version is available on the capsis platform (<https://capsis.cirad.fr/>, lasted access
737 the 12/06/2024) and can be downloaded from the "download" menu.

738 **Data availability**

739 Data from Mont Ventoux (2016-2017) at the seven sites are provided by URFM-INRAE
740 Avignon. The full dataset and site information can be accessed from
741 <https://doi.org/10.57745/B22AUG>.

742 DEM data are freely accessible and can be downloaded from <https://earthexplorer.usgs.gov/>
743 (last accessed 12/06/2024): the Global Multi-resolution Terrain Elevation Data 2010
744 (GMTED2010) (<https://doi.org/10.5066/F7J38R2N>) and the Shuttle Radar Topography
745 Mission (SRTM) 1 Arc-Second Global (<https://doi.org/10.5066/F7PR7TFT>).

746 Climate ERA5-Land data (<https://doi.org/10.24381/cds.e2161bac>), including global radiation,
747 are provided by Copernicus and can be directly downloaded from
748 <https://cds.climate.copernicus.eu/cdsapp#!/dataset/reanalysis-era5-land?tab=form> (last
749 accessed 12/06/2024).

750 **Author contribution**

751 Druel, A., Ruffault, J., Davi, H. and Martin-StPaul, N.K. designed the research and
752 performed the research. Druel, A. developed the scripts and the figures. Marloie, O. and
753 Martin-StPaul, N.K. collected the data on Mont Ventoux. Druel, A., Ruffault, J., Davi, H., De
754 Cáceres, M., Mouillot, F., François, C. and Martin-StPaul, N.K. interpreted the results. Druel,
755 A. led the writing of the manuscript with inputs from Ruffault, J., Chanzy, A., Marloie, O., De
756 Cáceres, M., Mouillot, F., François, C., Soudani, K., and Martin-StPaul, N.K. Finally, Druel,

757 [A., Ruffault, J., Oliosio, A., and Martin-StPaul, N.K., were particularly involved in the review.](#)

758 **Competing interests**

759 The authors declare that they have no conflict of interest.

760 **Acknowledgements**

761 This project received funding from the European Union's Horizon 2020 research and
762 innovation program under Grant Agreement No. 862221 (FORGENIUS). The authors would
763 also like to thank William Brunetto (URFM, INRAE, Avignon, France) for his help with data
764 acquisition on Mont Ventoux and Deborah Verfaillie for her help with proofreading.

765 **References**

- 766 Austin, M.P., Nicholls, A.O. and Margules, C.R.: Measurement of the realised qualitative
767 niche: Environmental niches of five Eucalyptus species. *Ecological Monographs*, 60(2): 161-
768 177, <https://doi.org/10.2307/1943043>, 1990.
- 769 Bailey, M. D., Nychka, D., Sengupta, M., Habte, A., Xie, Y., and Bandyopadhyay, S.:
770 Regridding uncertainty for statistical downscaling of solar radiation. *Adv. Stat. Clim.*
771 *Meteorol. Oceanogr.*, 9, 103–120, <https://doi.org/10.5194/asmo-9-103-2023>, 2023
- 772 Bedia, J., Herrera, S. and Gutiérrez, J.M.: Dangers of Using Global Bioclimatic Datasets
773 for Ecological Niche Modeling. Limitations for Future Climate Projections. *Global and*
774 *Planetary Change*, 107, 1-12, <http://dx.doi.org/10.1016/j.gloplacha.2013.04.005>, 2013.
- 775 Bird, R. E., and Hulstrom, R. L.: A simplified clear sky model for direct and diffuse
776 insolation on horizontal surfaces. *Solar Energy Research Institute*, TR-642-761, 1981.
- 777 [Bojanowski, J.S., Vrieling, A., and Skidmore, A.K.: A comparison of data sources for](#)
778 [creating a long-term time series of daily gridded solar radiation for Europe. *Sol. Energy*, 99,](#)
779 [152–171, <http://dx.doi.org/10.1016/j.solener.2013.11.007>, 2014.](#)
- 780 Bramer, I., Anderson, B.J., Bennie, J., Bladon, A.J., De Frenne, P., Hemming, D., Hill,
781 R.A., Kearney, M.R., Körner, C., Korstjens, A.H., Lenoir, J., Maclean, I.M.D., Marsh, C.D.,
782 Morecroft, M.D., Ohlemüller, R., Slater, H.D., Suggitt, A.J., Zellweger, F. and Gillingham,
783 P.K.: Advances in monitoring and modelling climate at ecologically relevant scales.
784 *Advances in Ecological Research*, 58, 101–161. <https://doi.org/10.1016/bs.aecr.2017.12.005>,
785 2018.
- 786 Brun, P., Zimmermann, N. E., Hari, C., Pellissier, L. and Karger, D. N.: CHELSA-
787 BIOCLIM+ A novel set of global climate-related predictors at kilometre-resolution. *EnviDat.*,
788 <https://www.doi.org/10.16904/envidat.332>, 2022.
- 789 [Buzzi, M.: \(2008\). Challenges in operational numerical weather prediction at high](#)
790 [resolution in complex terrain. ETH Zürich, PhD thesis, Veröffentlichung MeteoSchweiz Nr.](#)
791 [80, ISSN: 1422-1381, <https://doi.org/10.3929/ethz-a-005698833>, 2008.](#)
- 792 Cailleret, M. and Davi, H.: Effects of climate on diameter growth of co-occurring *Fagus*
793 *sylvatica* and *Abies alba* along an altitudinal gradient. *Trees*, 25:265–276.
794 <https://doi.org/10.1007/s00468-010-0503-0>, 2011.
- 795 Cailleret M., Nourtier M., Amm A., Durand-Gillmann M. and Davi H.: Drought-induced
796 decline and mortality of silver fir differ among three sites in Southern France. *Annals of*
797 *Forest Science*, 71, 643–657, 2013.
- 798 Carroll, C., Zielinski, W.J. and Noss, R.F.: Using presence-absence data to build and test
799 spatial habitat models for the Fisher in the Klamath region, U.S.A. *Conservation Biology*,
800 13(6): 1344-1359, <https://doi.org/10.1046/j.1523-1739.1999.98364.x>, 1999.
- 801 Clark, D.B., Palmer, M.W. and Clark, D.A.: Edaphic factors and the landscape-scale

802 distributions of tropical rain forest trees. *Ecology*, 80(8): 2662-2675,
803 [https://doi.org/10.1890/0012-9658\(1999\)080\[2662:EFATLS\]2.0.CO;2](https://doi.org/10.1890/0012-9658(1999)080[2662:EFATLS]2.0.CO;2), 1999.

804 Choat, B., Brodribb, T. J., Brodersen, C. R., Duursma, R. A., López, R. and Medlyn, B. E.:
805 Triggers of tree mortality under drought. *Nature*, 558(7711), 531–539.
806 <https://doi.org/10.1038/s41586-018-0240-x>, 2018.

807 Churkina, G., and Running, S. W.: Contrasting Climatic Controls on the Estimated
808 Productivity of Global Terrestrial Biomes. *Ecosystems*, 1(2), 206–215.
809 <https://doi.org/10.1007/s100219900016>, 1998.

810 Cochard, H., Pimont, F., Ruffault, J. & Martin-StPaul, N.: SurEau: a mechanistic model of
811 plant water relations under extreme drought. *Ann. For. Sci.*, 78,
812 <https://doi.org/10.1007/s13595-021-01067-y>, 2021.

813 [Coddington, O., Lean, J. L., Pilewskie, P., Snow, M. and Lindholm, D.: A Solar Irradiance](https://doi.org/10.1175/BAMS-D-14-00265.1)
814 [Climate Data Record. *Bull. Amer. Meteor. Soc.*, 97, 1265–1282,](https://doi.org/10.1175/BAMS-D-14-00265.1)
815 <https://doi.org/10.1175/BAMS-D-14-00265.1>, 2016.

816 Danielson, J.J., and Gesch, D.B.: Global multi-resolution terrain elevation data 2010
817 (GMTED2010): U.S. Geological Survey Open-File Report 2011–1073, 26 p.,
818 <https://doi.org/10.5066/F7J38R2N> (Downloaded on <https://earthexplorer.usgs.gov/> the 15-
819 10-2021), 2011.

820 Davi, H., Dufrêne, E., Granier, A., Le Dantec, V., Barbaroux, C., François, C. and Bréda,
821 N.: Modelling carbon and water cycles in a beech forest: Part II.: Validation of the main
822 processes from organ to stand scale. *Ecological Modelling*, 185, 387–405.
823 doi:10.1016/j.ecolmodel.2005.01.003, 2005.

824 Davi, H., Dufrêne, E., Francois, C., Le Maire, G., Loustau, D., Bosc, A., Rambal, S.,
825 Granier A. and Moors E.: Sensitivity of water and carbon fluxes to climate changes from
826 1960 to 2100 in European forest ecosystems. *Agric. For. Meteorol.*, 141, 35–56,
827 <https://doi.org/10.1016/j.agrformet.2006.09.003>, 2006.

828 Davi, H. and Cailleret, M.: Assessing drought-driven mortality trees with physiological
829 process-based models. *Agricultural and Forest Meteorology*, 232, 279–290,
830 <https://doi.org/10.1016/j.agrformet.2016.08.019>, 2017.

831 Davy, R. and Kusch, E.: Reconciling high resolution climate datasets using KrigR.
832 *Environ. Res. Lett.*, 16, 124040, <https://doi.org/10.1088/1748-9326/ac39bf>, 2021.

833 De Cáceres, M., Martínez-Vilalta, J., Coll, L., Llorens, P., Casals, P., Poyatos, R.,
834 Pausas, J.G. and Brotons, L.: Coupling a water balance model with forest inventory data to
835 predict drought stress: the role of forest structural changes vs. climate changes. *Agricultural*
836 *and Forest Meteorology*, 213: 77-90, <https://doi.org/10.1016/j.agrformet.2015.06.012>, 2015.

837 De Cáceres, M., Martin-StPaul, N., Turco, M., Cabon, A. and Granda, V.: Estimating daily
838 meteorological data and downscaling climate models over landscapes. *Environmental*

839 *Modelling and Software*, 108: 186-196, doi:10.1016/j.envsoft.2018.08.003, 2018.

840 De Cáceres M, Molowny-Horas R, Cabon A, Martínez-Vilalta J, Mencuccini M, García-
841 Valdés, R., Nadal-Sala, D., Sabaté, S., Martin-StPaul, N., Morin, X., D'Adamo, F., Batllori, E.
842 and Améztegui, A.: MEDFATE 2.9.3: A trait-enabled model to simulate Mediterranean forest
843 function and dynamics at regional scales. *Geoscientific Model Development*, 16, 3165–3201,
844 <https://doi.org/10.5194/gmd-16-3165-2023>, 2023.

845 De Jong, J.B.R.M.: Een karakterisering van de zonnestraling (A characterization of solar
846 radiation) in Nederland. Doctoral report, Eindhoven University of Technology, Netherlands,
847 97 + 67 pp., 1980.

848 Delpierre, N., Soudani, K., François, C., Le Maire, G., Bernhofer, C., Kutsch, W.,
849 Misson, L., Rambal, S., Vesala, T., and Dufrêne, E.: Quantifying the influence of climate and
850 biological drivers on the interannual variability of carbon exchanges in European forests
851 through process-based modelling. *Agric. For. Meteorol.*, 154–155, 99–112,
852 <https://doi.org/10.1016/j.agrformet.2011.10.010>, 2012.

853 Dirnbock, T., Dullinger, S., Gottfried, M., Ginzler, C. and Grabherr, G.: Mapping alpine
854 vegetation based on image analysis, topographic variables and Canonical Correspondance
855 Analysis. *Applied Vegetation Science*, 6: 85-96, [https://doi.org/10.1111/j.1654-
856 109X.2003.tb00567.x](https://doi.org/10.1111/j.1654-109X.2003.tb00567.x), 2003.

857 Dubayah, R. and Loechel, S.: Modeling topographic solar radiation using GOES data. *J.*
858 *Appl. Meteor.*, 36, 141–154, [https://doi.org/10.1175/1520-
859 0450\(1997\)036<0141:MTSRUG>2.0.CO;2](https://doi.org/10.1175/1520-0450(1997)036<0141:MTSRUG>2.0.CO;2), 1997.

860 Dufrêne, E., Davi, H., François, C., Maire, G. I., Dantec, V. L., and Granier, A.: Modelling
861 carbon and water cycles in a beech forest: Part I: Model description and uncertainty analysis
862 on modelled NEE. *Ecol. Model.*, 185, 407–436,
863 <https://doi.org/10.1016/j.ecolmodel.2005.01.004>, 2005.

864 Fealy, R. and Sweeney, J.: Statistical downscaling of temperature, radiation and potential
865 evapotranspiration to produce a multiple GCM ensemble mean for a selection of sites in
866 Ireland. *Irish Geography*, 41:1, 1-27, DOI: <https://doi.org/10.1080/00750770801909235>,
867 2008.

868 Fisher, J. B., Whittaker, R. J., and Malhi, Y.: ET come home: Potential evapotranspiration
869 in geographical ecology: ET come home. *Global Ecology and Biogeography*, 20(1), 1–18.
870 <https://doi.org/10.1111/j.1466-8238.2010.00578.x>, 2011.

871 Franklin, J.: Predicting the distribution of shrub species in southern California from climate
872 and terrain-derived variables. *Journal of Vegetation Science*, 9(5): 733-748,
873 <https://doi.org/10.2307/3237291>, 1998.

874 Corripio, J.G.: insol: Solar Radiation. R package version 1.2.2,
875 <https://www.meteoexploration.com/R/insol/> (last access 27/05/2024), 2020.

876 Granier, A., Breda, N., Biron, P. and Villette, S.: A lumped water balance model to
877 evaluate duration and intensity of drought constraints in forest stands. *Ecol. Model.*,
878 116:269–283, [https://doi.org/10.1016/S0304-3800\(98\)00205-1](https://doi.org/10.1016/S0304-3800(98)00205-1), 1999.

879 Granier, A., Reichstein, M., Bréda, N., Janssens, I. A., Falge, E., Ciais, P., Grünwald, T.,
880 Aubinet, M., Berbigier, P., Bernhofer, C., Buchmann, N., Facini, O., Grassi, G., Heinesch, B.,
881 Ilvesniemi, H., Keronen, P., Knohl, A., Köstner, B., Lagergren, F., Lindroth, A., Longdoz, B.,
882 Loustau, D., Mateus, J., Montagnani, L., Nys, C., Moors, E.J., Papale, D., Peiffer, M.,
883 Pilegaard, K., Pita, G., Pumpanen, J., Rambal, S., Rebmann, C., Rodrigues, A., Seufert, G.,
884 Tenhunen, J., Vesala, T. and Wang, Q.: Evidence for soil water control on carbon and water
885 dynamics in European forests during the extremely dry year: 2003. *Agricultural and Forest*
886 *Meteorology*, 143(1-2), 123-145. <https://doi.org/10.1016/j.agrformet.2006.12.004>, 2007.

887 Hammond, W. M., Yu, K., Wilson, L. A., Will, R. E., Anderegg, W. R. L. and Adams, H. D.:
888 Dead or dying? Quantifying the point of no return from hydraulic failure in drought-induced
889 tree mortality. *New Phytologist*, 223(4), 1834–1843, <https://doi.org/10.1111/nph.15922>,
890 2019.

891 Hernanz, A., Correa, C., Domínguez, M., Rodríguez-Guisado, E. and Rodríguez-Camino,
892 E.: Comparison of machine learning statistical downscaling and regional climate models for
893 temperature, precipitation, wind speed, humidity and radiation over Europe under present
894 conditions. *International Journal of Climatology*, 43, 13, 6065-6082,
895 <https://doi.org/10.1002/joc.8190>, 2023.

896 Hijmans, R.J., Cameron, S.E., Parra, J.L., Jones, P.G. and Jarvis, A.: Very high-
897 resolution interpolated climate surfaces for global land areas. *International Journal of*
898 *Climatology*, 25(15):1965-1978, <https://doi.org/10.1002/joc.1276>, 2005.

899 ~~I.E.A. (International Energy Agency): An Introduction to Meteorological Measurements~~
900 ~~and Data. Handling for Solar Energy Applications, Handbook Int. Energy Agency, Dept.~~
901 ~~Energy U.S.A., Washington D.C., 1978.~~

902 Jean, F., Davi, H., Oddou-Muratorio, S., Fady, B., Scotti, I., Scotti-Saintagne, C., Ruffault,
903 J., Journe, V., Clastre, P., Marloie, O., Brunetto, W., Correard, M., Gilg, O., Pringarve, M.,
904 Rei, F., Thevenet, J., Turion, N. and Pichot, C.: A 14-year series of leaf phenological data
905 collected for European beech (*Fagus sylvatica* L.) and silver fir (*Abies alba* Mill.) from their
906 geographic range margins in south-eastern France. *Annals of Forest Science*, (2023)80:35,
907 <https://doi.org/10.1186/s13595-023-01193-9>, 2023.

908 Klein, T.: The variability of stomatal sensitivity to leaf water potential across tree species
909 indicates a continuum between isohydric and anisohydric behaviours. *Funct. Ecol.*, 28,
910 1313–1320, <https://doi.org/10.1111/1365-2435.12289>, 2014.

911 Klucher, T.M.: Evaluation of models to predict insolation on tilted surfaces. Division of
912 *solar energy*, N.A.S.A. TM-78842, [https://doi.org/10.1016/0038-092X\(79\)90110-5](https://doi.org/10.1016/0038-092X(79)90110-5), 1978.

913 Lander, T.A., Klein, E.K., Roig, A. and Oddou-Muratorio, S.: Weak founder effects but
914 significant spatial genetic imprint of recent contraction and expansion of European beech
915 populations. *Heredity (Edinb)*, 126(3):491-504, doi: 10.1038/s41437-020-00387-5, 2021.

916 [Liston, G.E. and Elder, K.: A Meteorological Distribution System for High-Resolution](#)
917 [Terrestrial Modeling \(MicroMet\). *Journal of Hydrometeorology*, 7-2, 217-234,](#)
918 <https://doi.org/10.1175/JHM486.1>, 2006.

919 [Maraun, D., Wetterhall, F., Ireson, A., Chandler, R., Kendon, E. et al.: Precipitation](#)
920 [downscaling under climate change: Recent developments to bridge the gap between](#)
921 [dynamical models and the end user. *Reviews of Geophysics*, American Geophysical Union,](#)
922 [48 \(3\), https://doi.org/10.1029/2009RG000314](https://doi.org/10.1029/2009RG000314), 2010.

923 Martin-StPaul, N., Delzon, S. and Cochard, H.: Plant resistance to drought depends on
924 timely stomatal closure. *Ecology Letters*, 20(11), 1437–1447.
925 <https://doi.org/10.1111/ele.1285>, 2017.

926 Martin-StPaul, N., Ruffault, J., Guillemot, J., Barbero, R., Cochard, H., Cailleret, M.,
927 Cáceres, M. D., Dupuy, J.-L., Pimont, F., Torres-Ruiz, J. M., and Limousin, J.-M.: How much
928 does VPD drive tree water stress and forest disturbances? *Authorea*, Preprints.
929 <https://doi.org/10.22541/au.168147010.01270793/v1>, 2023.

930 Meentemeyer, R.K., Moody, A. and Franklin, J.: Landscape-scale patterns of shrub-
931 species abundance in California chaparral: The role of topographically mediated resource
932 gradients. *Plant Ecology*, 156: 19-41, <https://doi.org/10.1023/A:1011944805738>, 2001.

933 [Mira, M., Oliosio, A., Gallego-Elvira, B., Courault, D., Garrigues, S., Marloie, O., Hagolle,](#)
934 [O., Guillevic, P., and Boulet, G.: Uncertainty assessment of surface net radiation derived](#)
935 [from Landsat images. *Remote sensing of Environment*, 175, 251–270.](#)
936 <http://dx.doi.org/10.1016/j.rse.2015.12.054>, 2016.

937 Monteith, J. L.: Evaporation and surface temperature. *Quarterly Journal of the Royal*
938 *Meteorological Society*, 107(451), 1–27. <https://doi.org/10.1002/qj.49710745102>, 1981.

939 Moreno, M., Simioni, G., Cailleret, M., Ruffault, J., Badel, E., Carrière, S., Davi, H.,
940 Gavinet, J., Huc, R., Limousin, J.-M., Marloie, O., Martin, L., Rodríguez-Calcerrada, J.,
941 Vennetier, M. and Martin-StPaul, N.: Consistently lower sap velocity and growth over nine
942 years of rainfall exclusion in a Mediterranean mixed pine-oak forest. *Agricultural and Forest*
943 *Meteorology*, 308–309, 108472. <https://doi.org/10.1016/j.agrformet.2021.108472>, 2021.

944 [Müller, M. D. and Scherer, D.: A grid- and subgrid-scale radiation parametrization of](#)
945 [topographic effects for mesoscale weather forecast models. *Monthly Weather Review*, 133,](#)
946 [1431–1442, https://doi.org/10.1175/MWR2927.1](https://doi.org/10.1175/MWR2927.1), 2005.

947 Muñoz-Sabater, J., Dutra, E., Agustí-Panareda, A., Albergel, C., Arduini, G., Balsamo, G.,
948 Boussetta, S., Choulga, M., Harrigan, S., Hersbach, H., Martens, B., Miralles, D. G., Piles,
949 M., Rodríguez-Fernández, N. J., Zsoter, E., Buontempo, C., and Thépaut, J.-N.: ERA5-Land:

950 a state-of-the-art global reanalysis dataset for land applications. *Earth Syst. Sci. Data*, 13,
951 4349–4383, <https://doi.org/10.5194/essd-13-4349-2021>, 2021.

952 Oliphant, A. J., & Stoy, P. C.: An evaluation of semiempirical models for partitioning
953 photosynthetically active radiation into diffuse and direct beam components. *Journal of*
954 *Geophysical Research: Biogeosciences*, 123, 889–901,
955 <https://doi.org/10.1002/2017JG004370>, 2018.

956 Patsiou, T.S., Conti, E., Zimmermann, N.E., Theodoridis, S. and Randin, C.F.: Topo-
957 climatic microrefugia explain the persistence of a rare endemic plant in the Alps during the
958 last 21 millennia. *Global Change Biology*, 20(7):2286–2300,
959 <https://doi.org/10.1111/gcb.12515>, 2014.

960 Piedallu, C. and Gégout, J.-C.: Multiscale computation of solar radiation for predictive
961 vegetation modelling. *Ann. For. Sci.*, 64, 899-909, DOI: 10.1051/forest:2007072, 2007.

962 Piedallu, C. and Gégout, J.-C.: Efficient assessment of topographic solar radiation to
963 improve plant distribution models. *Agricultural and Forest Meteorology*, 148 (11), pp.1696-
964 1706., <https://doi.org/10.1016/j.agrformet.2008.06.001>, 2008.

965 Pierce, K.B., Lookingbill, T. and Urban, D.: A simple method for estimating potential
966 relative radiation (PRR) for landscape-scale vegetation analysis. *Landscape Ecology*, 20(2):
967 137-147, <https://doi.org/10.1007/s10980-004-1296-6>, 2005.

968 Poggio, L., De Sousa, L. M., Batjes, N. H., Heuvelink, G. B. M., Kempen, B., Ribeiro, E.,
969 and Rossiter, D.: SoilGrids 2.0: Producing soil information for the globe with quantified
970 spatial uncertainty. *Soil*, 7(1), 217–240. doi: 10.5194/soil-7-217-2021, 2021.

971 Randin, C. F., Engler, R., Normand, S., Zappa, M., Zimmermann, N. E., Pearman, P. B.,
972 Vittoz, P., Thuiller, W. and Guisan, A.: Climate change and plant distribution: local models
973 predict high-elevation persistence. *Global Change Biology*, 15(6), 1557-1569.
974 <https://doi.org/10.1111/j.1365-2486.2008.01766.x>, 2009.

975 Roderick, M. L.: Estimating the diffuse component from daily and monthly measurements
976 of global radiation. *Agricultural and Forest Meteorology*, 95, 169-185,
977 [https://doi.org/10.1016/S0168-1923\(99\)00028-3](https://doi.org/10.1016/S0168-1923(99)00028-3), 1999.

978 [Roerink, G.J., Bojanowski, J.S., de Wit, A.J.W., Eerens, H., Supit, I., Leo, O. and](#)
979 [Boogaard, H.L.: Evaluation of MSG-derived global radiation estimates for application in a](#)
980 [regional crop model. *Agric. For. Meteorol.*, 160, 36-47,](#)
981 [<https://doi.org/10.1016/j.agrformet.2012.02.006>, 2012.](#)

982 Ruffault, J., Martin-StPaul, N.K., Rambal, S. et Mouillot, F.: Differential regional
983 responses in drought length, intensity and timing to recent climate changes in a
984 Mediterranean forested ecosystem. *Climatic Change*, 117, 103–117,
985 <https://doi.org/10.1007/s10584-012-0559-5>, 2013.

986 Ruffault, J., Pimont, F., Cochard, H., Dupuy, J.-L., and Martin-StPaul, N.: SurEau-Ecos

987 v2.0: a trait-based plant hydraulics model for simulations of plant water status and drought-
988 induced mortality at the ecosystem level, *Geosci. Model Dev.*, 15, 5593–5626,
989 <https://doi.org/10.5194/gmd-15-5593-2022>, 2022.

990 Ruffault, J., Limousin, J.-M., Pimont, F., Dupuy, J.-L., De Cáceres, M., Cochard, H.,
991 Mouillot, F., Blackman, C.J., Torres-Ruiz, J.M., Parsons, R.A., Moreno, M., Delzon, S.,
992 Jansen, S., Olioso, A., Choat, B. and Martin-StPaul, N.: Plant hydraulic modelling of leaf and
993 canopy fuel moisture content reveals increasing vulnerability of a Mediterranean forest to
994 wildfires under extreme drought. *New Phytologist*, 237, 4, 1256-1269,
995 <https://doi.org/10.1111/nph.18614>, 2023.

996 [Senkova, A. V., Rontu, L., and Savijärvi, H.: Parametrization of orographic effects on](#)
997 [surface radiation in HIRLAM. *Tellus A: Dynamic Meteorology and Oceanography*, 59:3, 279-](#)
998 [291, <https://doi.org/10.1111/j.1600-0870.2007.00235.x>, 2007](#)

999 Spitters, C.J.T., Toussaint, H.A.J.M., and Goudriaan, J.: Separating the diffuse and direct
1000 component of global radiation and its implications for modeling canopy photosynthesis Part I.
1001 Components of incoming radiation. *Agr. and Forest Met.*, 38(1-3), 217-229,
1002 [https://doi.org/10.1016/0168-1923\(86\)90060-2](https://doi.org/10.1016/0168-1923(86)90060-2), 1986.

1003 Shuttle Radar Topography Mission (SRTM): 1 Arc-Second Global (2013).
1004 <https://doi.org/10.5066/F7PR7TFT> (Downloaded on <https://earthexplorer.usgs.gov/> the 15-
1005 10-2021), 2013.

1006 Stéfanon, M., Martin-StPaul, N. K., Leadley, P., Bastin, S., Dell'Aquila, A., Drobinski, P.,
1007 and Gallardo, C.: Testing climate models using an impact model: What are the advantages?
1008 *Climatic Change*, 131(4), 649–661, <https://doi.org/10.1007/s10584-015-1412-4>, 2015.

1009 Tappeiner, U., Tasser, E. and Tappeiner, G.: Modelling vegetation patterns using natural
1010 and anthropogenic influence factors: preliminary experience with a GIS based model applied
1011 to an Alpine area. *Ecological Modelling*, 113(1-3): 225-237, <https://doi.org/10.1016/S0304->
1012 [3800\(98\)00145-8](https://doi.org/10.1016/S0304-3800(98)00145-8), 1998.

1013 [Widén, J. and Munkhammar, J.: Solar Radiation Theory. *Uppsala University, Department*](#)
1014 [of Engineering Sciences, <https://doi.org/10.33063/diva-381852>, 2019.](#)

1015 –Zimmermann, N.E. and Kienast, F.: Predictive mapping of alpine grasslands in
1016 Switzerland: Species versus community approach. *Journal of Vegetation Science*, 10(4):
1017 469-482, <https://doi.org/10.2307/3237182>, 1999.